THE SIGNIFICANCE OF MICROWAVE OBSERVATIONS FOR THE PLANETS

Imke de PATER

Astronomy Department, Campbell Hall 601, University of California, Berkeley, CA 94720, USA

NORTH-HOLLAND

PHYSICS REPORTS (Review Section of Physics Letters) 200, No. 1 (1991) 1–50. North-Holland

THE SIGNIFICANCE OF MICROWAVE OBSERVATIONS FOR THE PLANETS

Imke de PATER

Astronomy Department, Campbell Hall 601, University of California, Berkeley, CA 94720, USA

Editor: D.N. Schramm Received June 1990

Contents:

Single orders for this issue

PHYSICS REPORTS (Review Section of Physics Letters) 200, No. 1 (1991) 1–50.

Copies of this issue may be obtained at the price given below. All orders should be sent directly to the Publisher. Orders must be accompanied by check.

Single issue price Dfl. 37.00, postage included.

0 370-1573/91/$17.50

Abstract:

A review of radio observations of the giant and terrestrial planets is presented, together with a discussion as to how our understanding of the planets' surfaces, atmospheres and magnetospheres has improved with help of these data.

Giant planet atmospheres. The radio spectra and resolved images of the four giant planets are compared. Jupiter and Saturn are very much alike: NH_3 gas is depleted compared to what would be expected for a solar nitrogen abundance by a factor of ~5 at $P \leq 1$–2 bar, and enhanced by ~1.5 at $P > 2$ bar on Jupiter and by 3–4 at $P > 4$–5 bar on Saturn. Bright bands across the planetary disks imply a latitudinal variation in the precise ammonia abundance. Uranus and Neptune are very different from the former two planets, in that they exhibit a depletion of NH_3 gas by about two orders of magnitude over a large altitude range in the atmosphere. Uranus shows a large pole-to-equator gradient in brightness temperature.

The loss of NH_3 gas in all four planetary atmospheres is most likely due to the formation of NH_4SH. This requires the H_2S abundance in Jupiter and Saturn to be enhanced by a factor of 6–7 and 10–15 respectively above the solar value, and in Uranus and Neptune by over two orders of magnitude. The NH_3 and H_2S abundances derived from radio data support the "core-instability" models on planetary formation by Pollack and Bodenheimer [1989].

The latitudinal variation in the NH_3 abundance on the planets suggests differences in the location of the NH_4SH cloud layers and hence the dynamics of the planets.

Jupiter's synchrotron radiation. Radio observations of Jupiter's synchrotron radiation have led to a detailed model of Jupiter's inner magnetosphere with electron distributions. The satellites Thebe and Amalthea cause the electrons to be confined to the magnetic equatorial plane. Energy degradation of the electrons by dust in Jupiter's ring harden the electron spectrum considerably. A "hot spot" in Jupiter's radiation belts can partly be explained by the multipole character of Jupiter's field and a dusk–dawn electric field over the magnetosphere. From a comparison between the time variability in Jupiter's synchrotron radiation and that seen in solar wind parameters, it appears that the solar wind does influence the supply and/or loss of electrons to Jupiter's inner magnetosphere.

Terrestrial planets. Microwave observations of the terrestrial planets pertain to depths of approximately ten wavelengths. Spectra and resolved images of the planets contain information on the composition and compaction of the surface layers. Typically, the planets' crusts are overlain with a few centimeters dust. The polar regions on Mars are much colder than the surrounding areas. The highlands on Venus have a lower emissivity and hence higher dielectric constant than the disk-averaged value; this implies the presence of substantial amounts of minerals and sulfides close to the surface. Mercury exhibits "hot spots" in its sub-surface layers, due to the 3/2 orbital resonance and large orbital eccentricity.

Observations at millimeter wavelengths, in particular in rotational transitions of the CO line, are used to derive the temperature gradient in Venus and Mars' atmospheres, and the CO abundance as a function of altitude. The CO abundance on Mars is much lower than expected from recombination of CO and O. Apparently, some catalyst is present to speed up the recombination process. On Venus we find most of the CO on the nightside, while it is formed on the dayside hemisphere. Large thermal winds may carry the CO from the day to the nightside.

General introduction

Observations of the giant planets (Jupiter, Saturn, Uranus and Neptune) at millimeter–centimeter wavelengths have contributed significantly to our knowledge of the composition and structure of the planets' atmospheres and the magnetic field topology and distribution of energetic electrons in Jupiter's inner magnetosphere. At radio wavelengths we receive thermal or blackbody radiation from the planets' atmospheres. From Jupiter we also receive non-thermal or synchrotron radiation at centimeter wavelengths, which is emitted by energetic electrons trapped in its inner magnetosphere. The thermal radiation from all planets increases with decreasing wavelength (λ^{-2} dependence). The non-thermal flux density from Jupiter is more or less constant with wavelength, so that its relative contribution to the total emission from the planet increases with wavelength.

The thermal or blackbody radiation from the terrestrial planets (Mars, Venus and Mercury) at millimeter–centimeter wavelengths contains information on the subsurface layers of these bodies, as well as their atmospheres (Mars, Venus).

In the first chapter of this paper radio spectra and images of the giant planets are discussed. The second chapter gives a review of radio observations of Jupiter's synchrotron radiation. The third chapter contains a discussion of microwave observations of the terrestrial planets.

This paper shows many similarities to the paper Radio images of the planets, [de Pater 1990]. The single dish data of planets however, are discussed in more detail in this paper, and so is the time variability in the data.

The basic principles of radio astronomy and interferometry have been described by, e.g., Kraus [1986], Rohlfs [1986], Thompson et al. [1986], and Perley et al. [1989]; the reader is referred to these papers for general background in radio astronomy. A tutorial on image reconstruction of planets was given by de Pater [1990], and will not be repeated here.

1. Giant planets; thermal radiation

1.1. Introduction

At radio wavelengths in the millimeter–centimeter regime one generally probes regions in planetary atmospheres which are inaccessible to optical or infrared wavelengths. One typically probes pressure levels of ~0.5–10 bar in Jupiter and Saturn's atmospheres, and down to 50–100 bar in Uranus and Neptune. Much information is contained in the planet's radio spectrum: a graph of the disk-averaged brightness temperature of the planet as a function of wavelength. These spectra generally show an increase in brightness temperature with increasing wavelength beyond 1.3 cm, due to the combined effect of a decrease in opacity at longer wavelengths, and an increase in temperature at increasing depth in the planet. At millimeter–centimeter wavelengths the main source of opacity is ammonia gas, which has a broad absorption band at 1.3 cm. At longer wavelengths (typically >10 cm) absorption by water vapor and droplets becomes important, while at short millimeter wavelengths the contribution of collision induced absorption by hydrogen gas becomes noticeable.

Radio spectra of the planets can be interpreted by comparison of observed spectra with synthetic spectra, obtained by integrating the equation of radiative transfer through a model atmosphere. The most recent and complete study on a comparison between radio spectra and model atmosphere calculations for all four planets was published by de Pater and Massie [1985]. At first approximation the spectra of both Jupiter and Saturn resemble those expected for a solar composition atmosphere, while the spectra of Uranus and Neptune indicate a depletion of ammonia gas compared to the solar value by about two orders of magnitude [Gulkis et al. 1978; de Pater and Massie 1985]. Resolved images of both Jupiter and Saturn show bands of enhanced brightness temperature on their disks [de Pater and Dickel 1986, 1989; Grossman et al. 1989], implying latitudinal variations in the precise ammonia abundance. Uranus shows a brightening towards the visible (south) pole (e.g., Jaffe et al. [1984], de Pater and Gulkis [1988]); images of Neptune have too low a resolution at this time to infer latitudinal variations in brightness temperature. The spectra and two-dimensional images of each planet are discussed in sections 1.3–1.6. Section 1.7 contains a discussion of the relation between the atmospheric composition to models on planetary formation.

1.2. Model atmosphere simulations

To extract information on the planets' deep atmospheres from their radio spectra, one needs a reliable computer code to simulate the thermal radio emission from a model atmosphere. In this section I will summarize the most recent model atmosphere program used to simulate radio observations [Briggs and Sackett 1989; de Pater et al. 1989].

The disk-averaged brightness temperature at radio wavelengths, T_D, is calculated by a numerical integration over optical depth, τ, and position μ on the disk. The disk-averaged brightness, $B_\nu(T_D)$, is given by

$$B_\nu(T_D) = 2 \int_0^1 \int_0^\infty B_\nu(T) \exp(-\tau/\mu)\, d(\tau/\mu)\, d\mu\,. \quad (1)$$

The brightness $B_\nu(T)$ is given by the Planck function, and optical depth $\tau_\nu(z)$ is the integral of the total absorption coefficient over the altitude range z at frequency ν. The parameter μ is the cosine of the angle between the line of sight and local vertical. Details on the equation and absorption coefficients can be found in de Pater and Massie [1985]. The latter authors caution against the "blind" use of the Ben Reuven line shape profile, generally used to approximate the shape of the ammonia lines centered near 1.3 cm. Based upon a comparison of model atmosphere calculations with all four giant planets, they suggest that the line profile at millimeter wavelengths probably resembles that of a (slightly modified) Van Vleck–Weisskopf rather than a Ben Reuven profile. The Ben Reuven representation is probably right at centimeter wavelengths [Steffes and Jenkins 1987].

Before the integration in eq. (1) can be carried out, the atmospheric structure, as composition and temperature–pressure curve, needs to be defined. Since the temperature, pressure and composition of an atmosphere are all related, de Pater et al. [1989] calculate the atmospheric structure, after specification of the temperature, pressure, and composition of one mole of gas at some deep level in the atmosphere (well below the formation of clouds). The model then steps up in altitude from the base level and the new temperature is calculated assuming a dry adiabatic lapse rate, and the new pressure by using hydrostatic equilibrium. The partial pressures of the trace gases in the atmosphere are compared to the saturation vapor pressures and if the partial pressure exceeds the latter value, a cloud of that condensate forms.

The following cloud layers are expected to form in the giant planet atmospheres: aqueous ammonia solution cloud (H_2O–NH_3–H_2S) at relatively deep levels in the atmosphere. Stepping up in altitude we find water ice, ammonium hydrosulfide solid, ammonia ice, hydrogen sulfide ice, and methane ice (only on Uranus and Neptune is the temperature cold enough for methane ice to form). Since the NH_4SH cloud forms as a result of a reaction between NH_3 and H_2S gases, the test for NH_4SH cloud formation is that the equilibrium constant of the reaction is exceeded. Both NH_3 and H_2S are reduced in equal molar quantities until the product of their atmospheric pressures equals the equilibrium constant. The model then steps up in altitude using either the dry or the appropriate wet adiabat. As the trace gases are removed from the atmosphere by condensation, "dry" air (an H_2–He mixture) is entrained into the parcel to ensure the mixing ratios add up to one. This cycle is repeated until the tropopause temperature is reached. For more specifics on the cloud formation, the reader is referred to the papers by Romani [1986] and de Pater et al. [1989].

1.3. Jupiter

Radio signals from Jupiter were first detected in 1955 at a frequency of 22.2 MHz [Burke and Franklin 1955]. This emission was sporadic in character, and confined to frequencies less than 40 MHz. It is likely due to cyclotron radiation from electrons with mirror points close to Jupiter's ionosphere. Excellent review papers on this topic are written by, e.g., Carr and Desch [1976], and Carr et al. [1983].

A detailed historic review on radio observations of Jupiter at microwavelengths was given by Berge and Gulkis [1976]. They noted that the first detection of microwave radiation from the planet was made in 1956 at 3 cm wavelength by Mayer et al. [1958]. The measured flux density corresponds to a black body temperature of about 140 K. In subsequent years, observations at longer wavelengths were

conducted, which yielded temperatures of a few thousand degrees at wavelengths $\lambda \gtrsim 10$ cm. Even though one expects a temperature gradient in an atmosphere, the measured spectrum was too steep to be caused by a reasonable atmospheric gradient (as, e.g., adiabatic gradient). Interferometric observations by Radhakrishnan and Roberts [1960] in 1960 at a wavelength of 31 cm, and a year later by Morris and Berge [1962] at 31 and 22 cm, showed that the radiation was ~30% linearly polarized at both wavelengths and had a linear extent roughly 3 times the planet's diameter in the equatorial direction, while the north–south extent agreed with the planetary diameter. This led to the suggestion that Jupiter's radio emission at wavelengths $\gtrsim$6 cm was dominated by synchrotron radiation, emitted by high energy electrons in a Jovian Van Allen belt. Emission at shorter wavelengths is dominated by the thermal radiation from the planet's atmosphere.

The significance of the synchrotron radiation as a probe for Jupiter's inner magnetosphere will be discussed in chapter 2. In this section we concentrate on the thermal emission; however, we first need to spend a few words on how to separate the thermal component from Jupiter's non-thermal emission. This topic has been addressed in detail by Berge and Gulkis [1976], and was extended by de Pater et al. [1982]. The most widely used technique is based upon the polarization properties of the two emission components. One assumes that the thermal emission is essentially unpolarized, and that the degree of polarization in the synchrotron radiation is 22% at all wavelengths. This number was defined from the degree of polarization at long wavelengths, averaged over Jupiter's rotation; at long wavelengths the thermal contribution is negligible. It was assumed that the degree of linear polarization remains constant at shorter wavelengths; a fairly good assumption, since de Pater [1981a] showed later that it

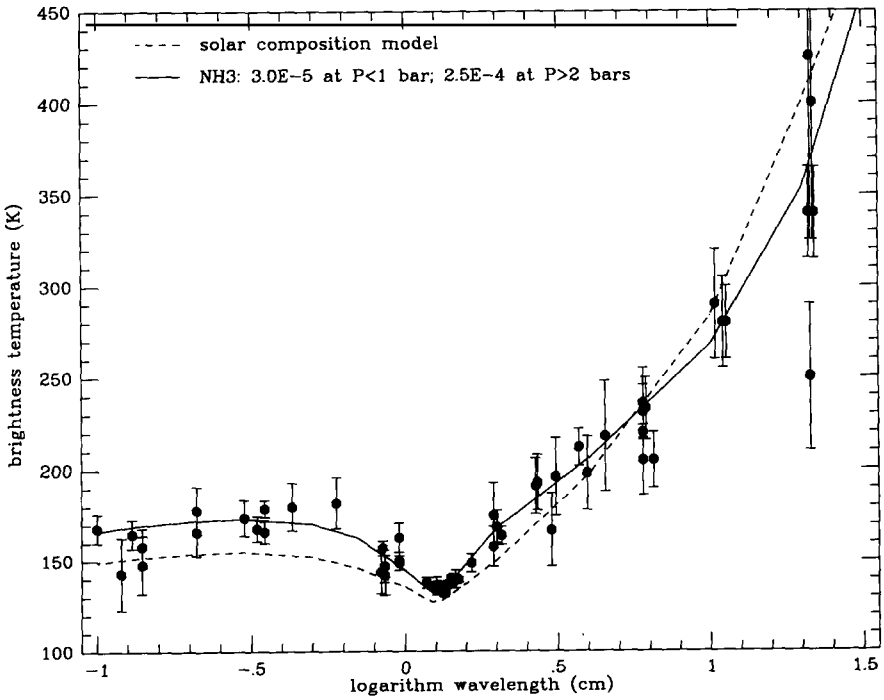

Fig. 1. Jupiter's radio spectrum with superimposed various model atmosphere calculations. Dashed line: solar composition atmosphere. Solid line: NH_3: 3×10^{-5} at $P < 1$ bar and 2.5×10^{-4} at $P > 2$ bar.

decreases by only ~2% between 20 and 6 cm. When high resolution images were obtained one could in principle separate the thermal and non-thermal contributions visually; however, since the region subtended by the disk is also partly influenced by synchrotron radiation more refined models needed to be used. De Pater et al. [1982] used de Pater's [1981a, b] model calculations together with high resolution images of the planet to determine more accurate values for the thermal flux density at wavelengths of 6, 11 and 21 cm.

Figure 1 shows a disk-averaged spectrum of Jupiter, with data taken from de Pater and Massie [1985] and references therein, and Klein and Gulkis [1978]. Superimposed are model atmosphere calculations after de Pater and Massie [1985] (models after de Pater and Massie always have a Ben Reuven line shape profile for NH_3 gas at centimeter wavelengths, and a modified Van Vleck–Weiskopf line shape at millimeter wavelengths). The dashed line is for a solar composition model*), and the solid line is for a model atmosphere in which ammonia gas is depleted compared to the solar nitrogen value by a factor of ~5 at $P < 1$ bar, and enhanced by a factor of 1.5 at $P > 2$ bar. In addition, NH_3 gas is subsaturated at $P \lesssim 0.6$ bar, to fit the radio spectrum near 1.3 cm. The latter model provides a good fit to the data. The loss in NH_3 gas at $1 < P < 2$ bar is probably due to the formation of an NH_4SH cloud. The existence of such a cloud was first postulated by Lewis [1969], to explain the apparent non-detection of H_2S gas in Jupiter's atmosphere. If indeed the NH_3 mixing ratio drops by a factor of about 8 due to the formation of an NH_4SH cloud, H_2S needs to be enhanced by a factor of 6–7 compared to the solar value [de Pater 1986]. This is compatible with theories on the formation and evolution of the giant planets [Hubbard 1984; Pollack and Bodenheimer 1989]. The subsaturation of ammonia gas at $P \lesssim 0.6$ bar is probably due to photolysis.

High resolution radio images of the planet at 2 and 6 cm wavelength are displayed in fig. 2a–d (from de Pater and Dickel [1986]). The resolution is 1.2″ and 2″ respectively. The images show bright horizontal bands across the disk, which coincide with the brown belts seen at visible and IR wavelengths. These bands have a higher brightness temperature, which most likely is due to a depletion in ammonia gas relative to the zonal regions. Figure 3 shows a summary of the atmospheric structure in Jupiter's North Equatorial Belt (NEB) and Equatorial Zone (EZ) (from de Pater [1986]). The NH_3 gas is enhanced by a factor of 1.5 at $P > 2.2$ bar. We see a gradual decrease in NH_3 gas between 2 and 1 bar, where in the NEB the gas is depleted over a small altitude range by a factor about 10, and in the EZ by a factor of about 5 over a larger altitude range. The depletion in both regions is probably caused by the formation of an NH_4SH cloud layer, which extends over a larger altitude range in the zone than the belt. At $P < 0.6$ bar, NH_3 is condensed out, and partially destroyed by photodissociation effects.

De Pater [1986] shows that the difference in latent heat release upon formation of an extensive NH_4SH cloud in the EZ, versus a three-times smaller cloud in the NEB is 3–4 K, enough to drive the zonal winds observed on the planet. This theory predicts the winds to extend down to a depth of ~2 bar. It further confirms the historical picture of rising gas in the warmer zones, with subsidence in the belts. With the smaller NH_3 gas reservoir above the belts, the NH_3 ice clouds are expected to be thinner in belts than in zones. This general cloud picture is in agreement with the structure suggested by West et al. [1986] based upon ground-based and spacecraft data at visible and IR wavelengths. Note, however, the difference between the two observing techniques: the radio data probe directly the gas from which the clouds are formed, while IR and visible data are sensitive to "a" cloud layer. Hence, together, the data contain a full picture of Jupiter's cloud structure.

*) The solar mixing ratios: CH_4/H_2, 8.35×10^{-4}; NH_3/H_2, 1.74×10^{-4}; H_2O/H_2, 1.38×10^{-3}; H_2S/H_2, 3.76×10^{-5}.

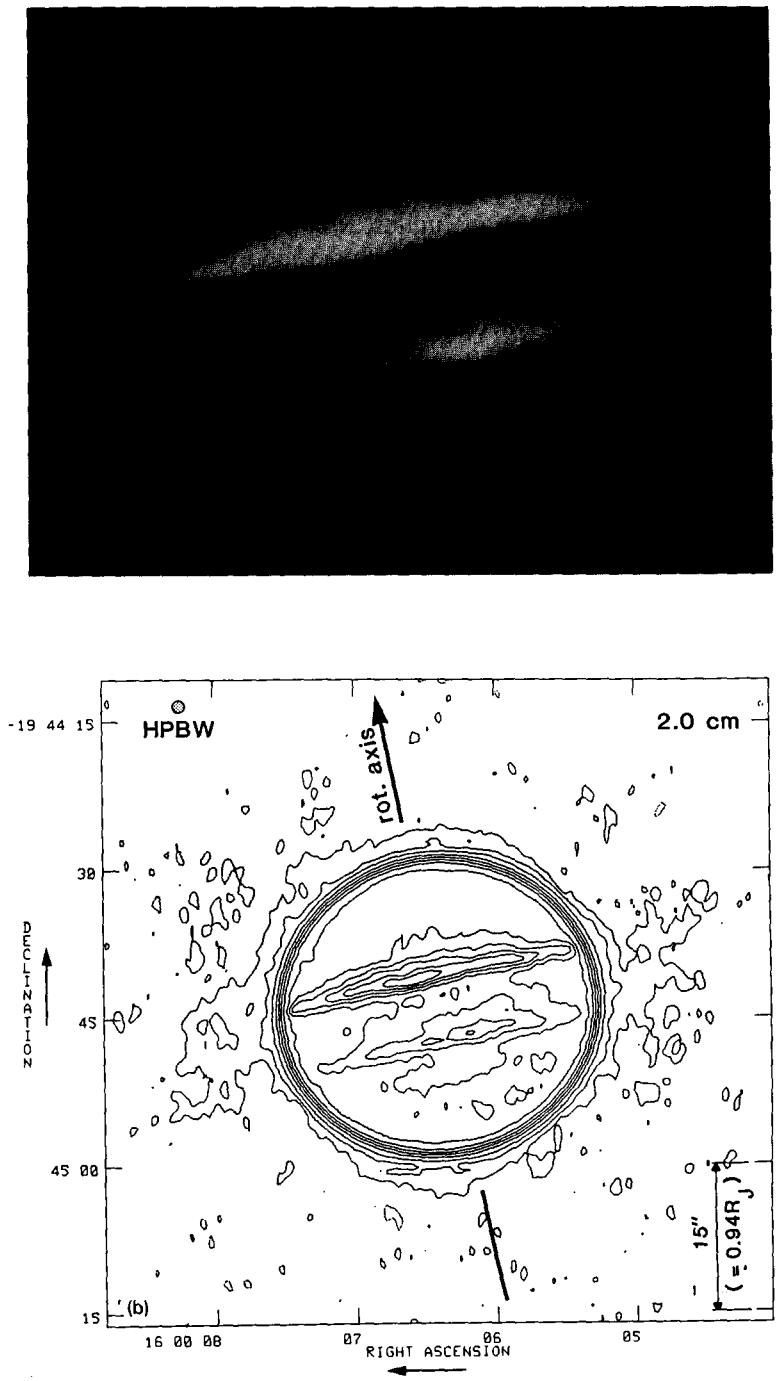

Fig. 2. (a) a radio photo, and (b) a contour map of Jupiter at a wavelength of 2 cm. Contour values are: 1.8, 5, 9, 18, 44, 71, 98, 124, 151, 160, 168, and 174 K. (c) a contour map of Jupiter's total intensity at 6 cm. Contour levels are: 8.5, 14, 20, 28, 43, 57, 71, 114, 157, 200, 242, 256, 270, and 279 K. (d) a contour map of Jupiter's thermal emission at 6 cm, obtained by subtracting a scaled map of the polarized flux density from the total intensity map. Contour values are; 8, 13, 19, 26, 40, 53, 66, 106, 146, 185, 225, 238, 251, and 259 K. On all contour maps, negative values, with the same absolute levels, are indicated by dashed contours. (Results are from de Pater and Dickel [1986].)

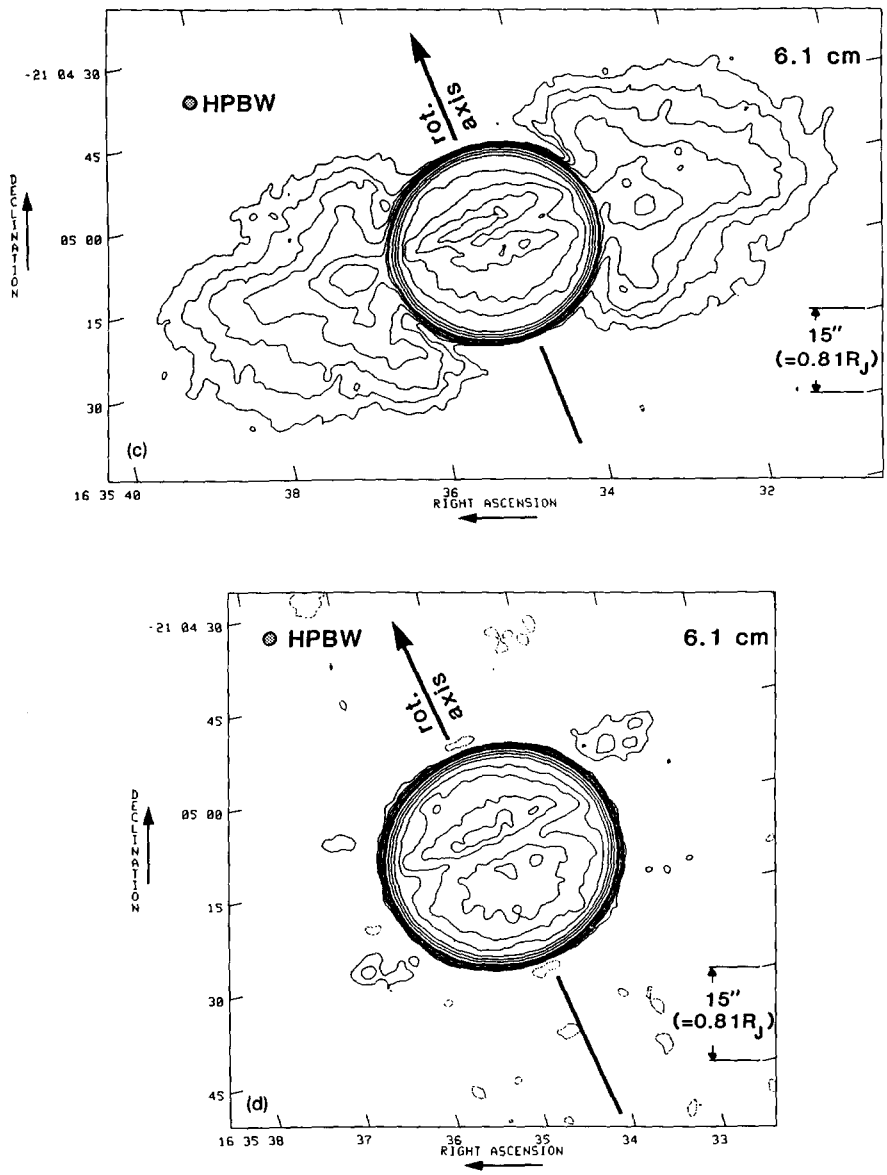

Fig. 2. (Contd)

1.4. Saturn

1.4.1. Atmosphere

The results of microwave observations of Saturn have been compiled by Klein et al. [1978]. Since most observations have been obtained with single dish telescopes, which have a very low spatial resolution, the flux density of the entire Saturnian system was recorded. Measurements obtained with radio interferometers provided some strong constraints on the microwave properties of Saturn's ring

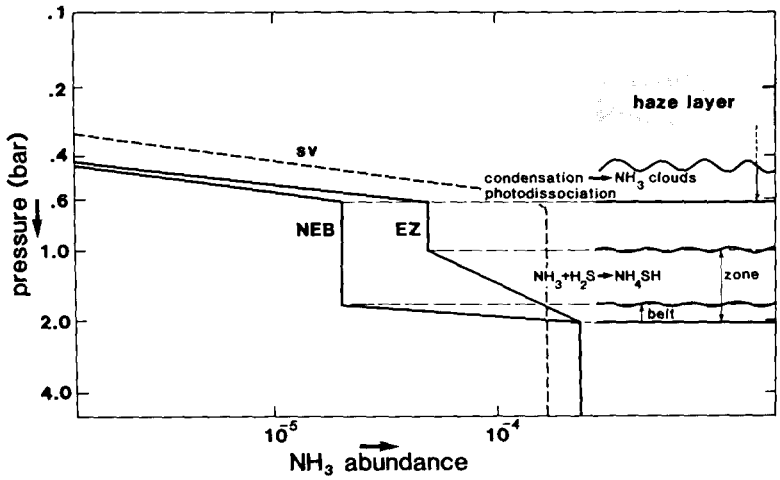

Fig. 3. The altitude distribution of ammonia gas in Jupiter's atmosphere, in the NEB and EZ. The various cloud layers are sketched at the right side; the saturated vapor curve for ammonia gas of solar concentration is indicated by the line sv. (Results from de Pater [1986].)

system. Klein et al. [1978] used this information to develop a simple model for the influence of the planet's rings on its microwave spectrum, and corrected the radio data for it. The resulting thermal spectrum of Saturn is shown in fig. 4 (the data are complemented with data by Dowling et al. [1987], Grossman et al. [1989], Briggs and Sackett [1989], and de Pater and Dickel [1989]). Superimposed is a

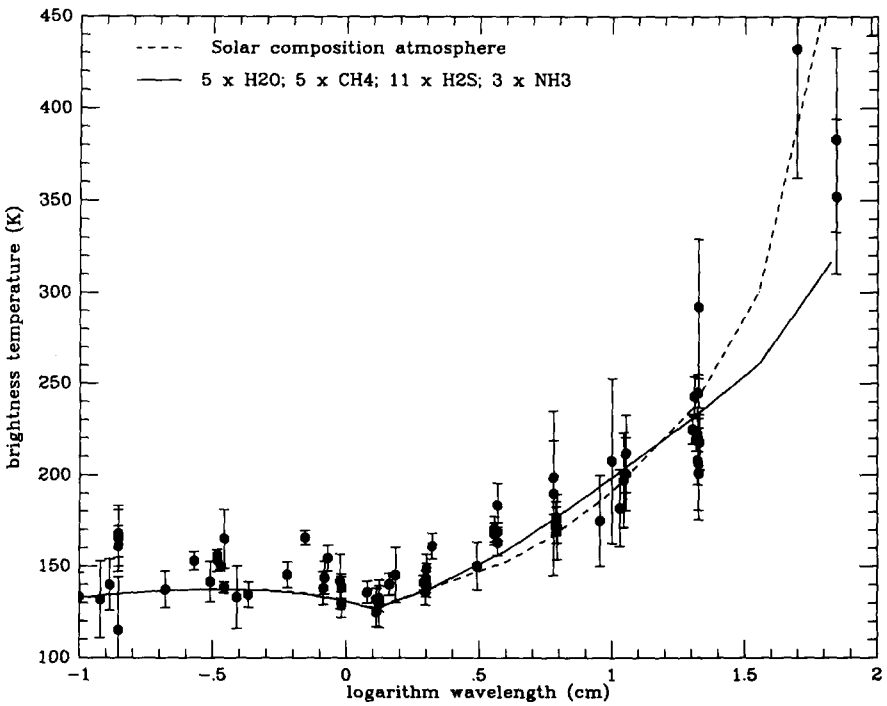

Fig. 4. Saturn's radio spectrum, with superimposed model atmosphere calculations (after Briggs and Sackett [1989]). Dashed line: solar composition atmosphere. Solid line: an atmosphere in which methane gas and water are enhanced by a factor of 5, ammonia gas by a factor of 3, and H_2S gas by a factor of 11 above solar.

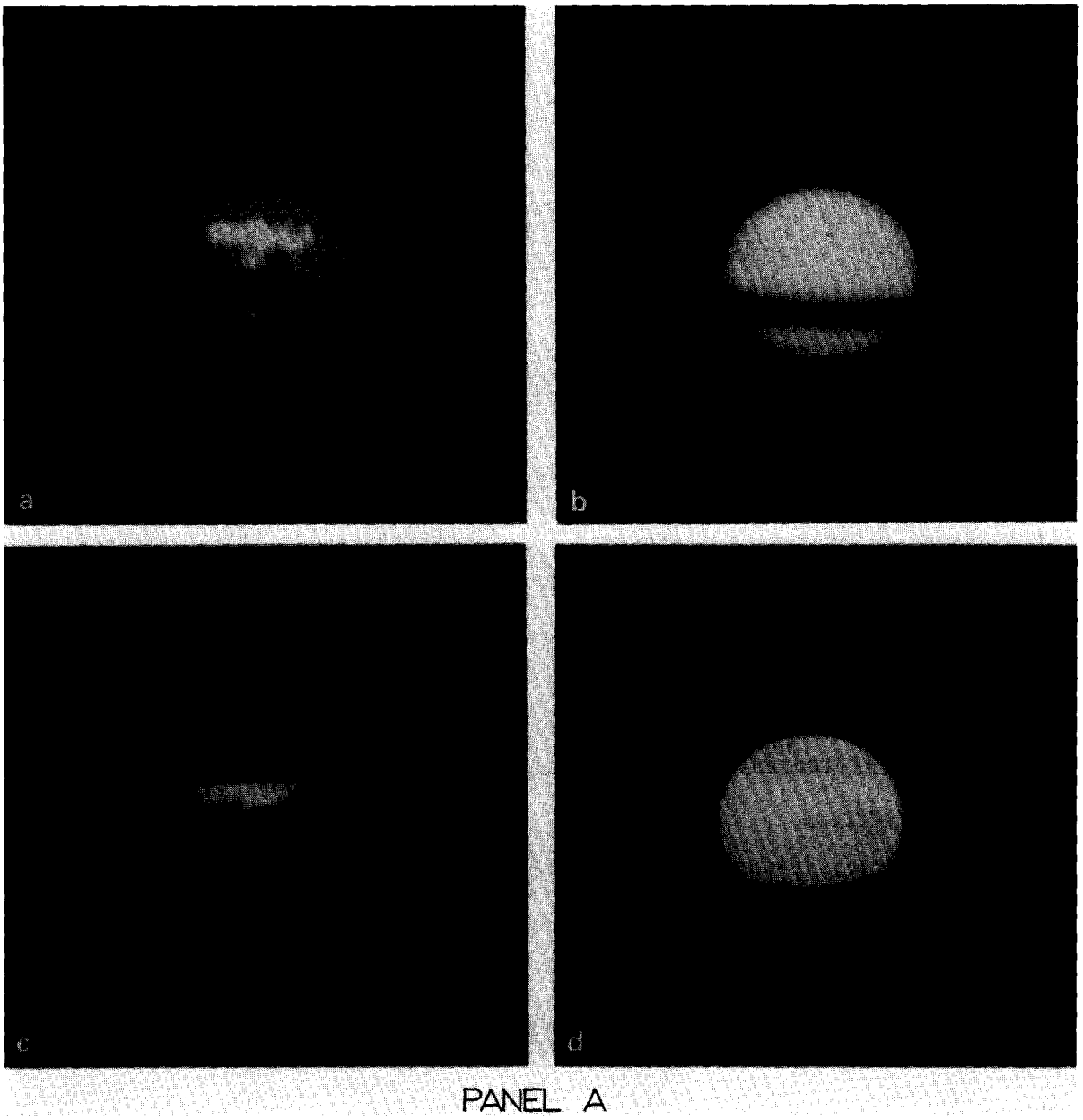

Fig. 5. Radio images of Saturn (from de Pater and Dickel [1989]), at 2 and 6 cm at different ring inclination angles B. Panel A shows radio photos of the images, panel B the contour maps. The resolution in all images is 1.5″. (a) image at $\lambda = 6$ cm, $B = 5.8°$. Contour values are: 2.7, 5.4, 9.2, 18.4, 45.8, 73.4, 100.9, 128.5, 155.9, 165.2, 174.3, and 179.8 K. (b) image at $\lambda = 2$ cm, $B = 12.5°$. Contour values are: 2.2, 3.4, 4.5, 6.0, 7.5, 11.2, 14.9, 37.3, 59.7, 82.1, 104.5, 126.9, 134.3, 141.8, and 144.8 K. (c) image at $\lambda = 6$ cm, $B = 20°$. Contour values are: 1.9, 3.8, 5.8, 7.7, 9.6, 13.5, 19.2, 48.1, 77.0, 105.8, 134.7, 163.5, 173.1, 178.9, 184.7, and 188.6 K. (d) image at $\lambda = 2$ cm, $B = 26°$. Contour values are: 0.7, 1.5, 3.0, 4.4, 5.8, 7.3, 10.2, 14.5, 36.3, 58.1, 80.0, 101.7, 123.6, 130.8, 135.2, 139.6, and 142.5 K. Negative contour values, with the same absolute levels, are indicated by dashed contours. The images were taken in August 1981, January 1982, January 1984, and December 1986, respectively.

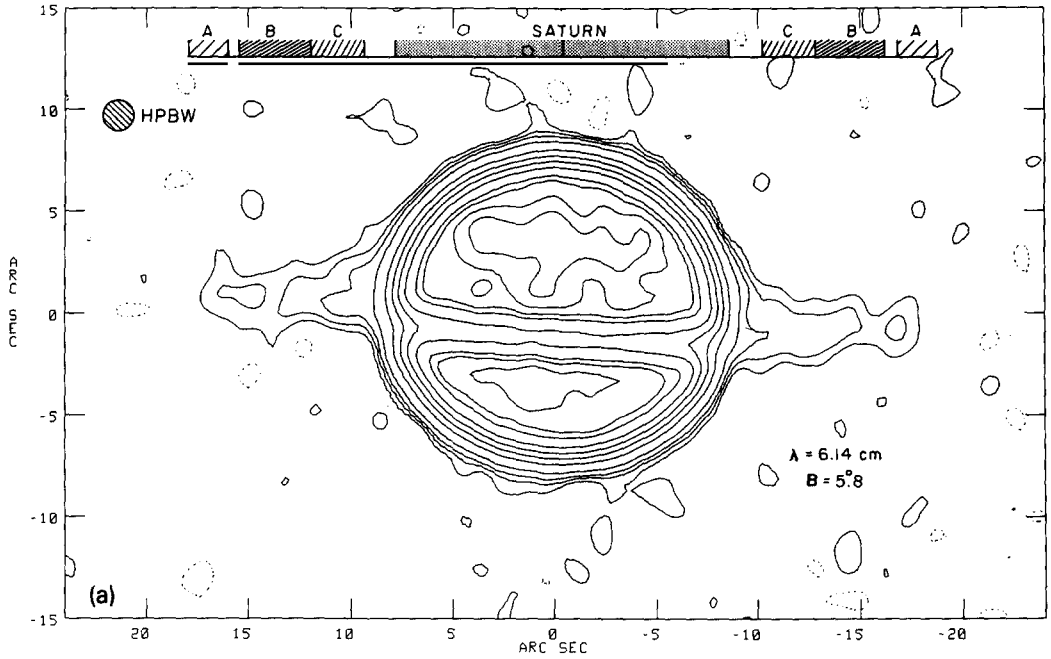

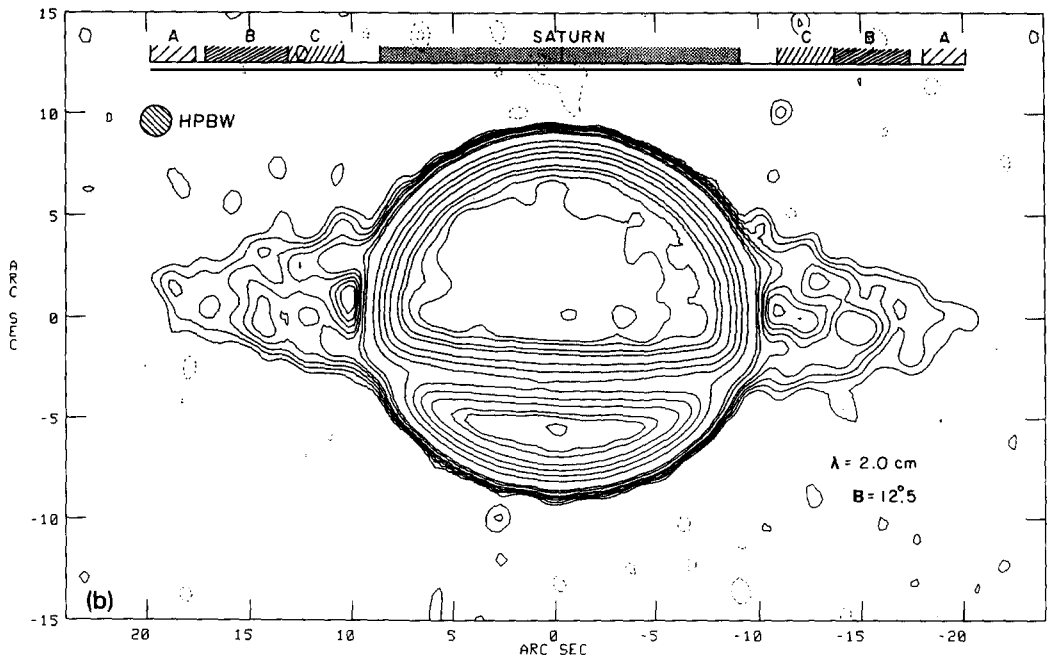

Fig. 5. Panel B. Radio images of Saturn; contour maps (a) and (b).

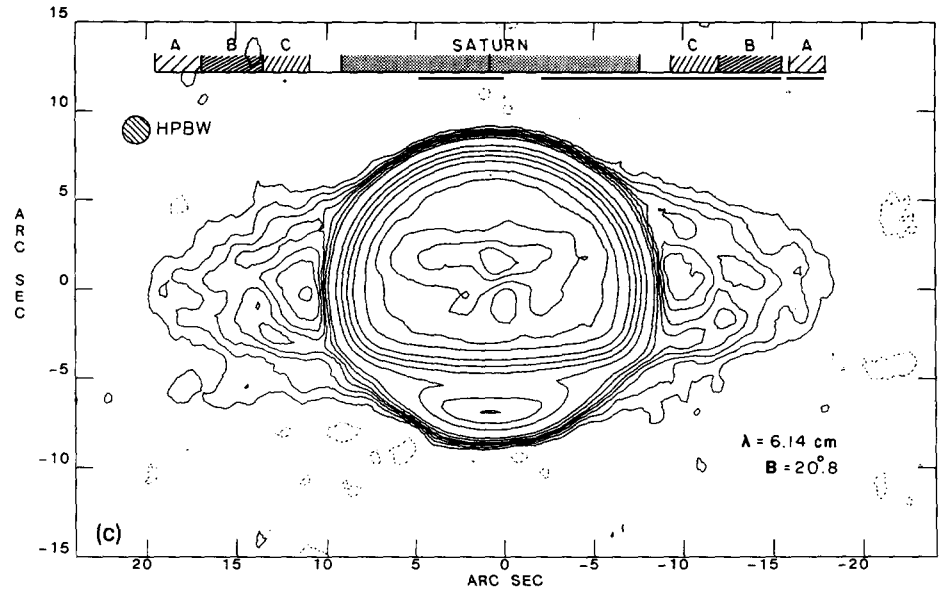

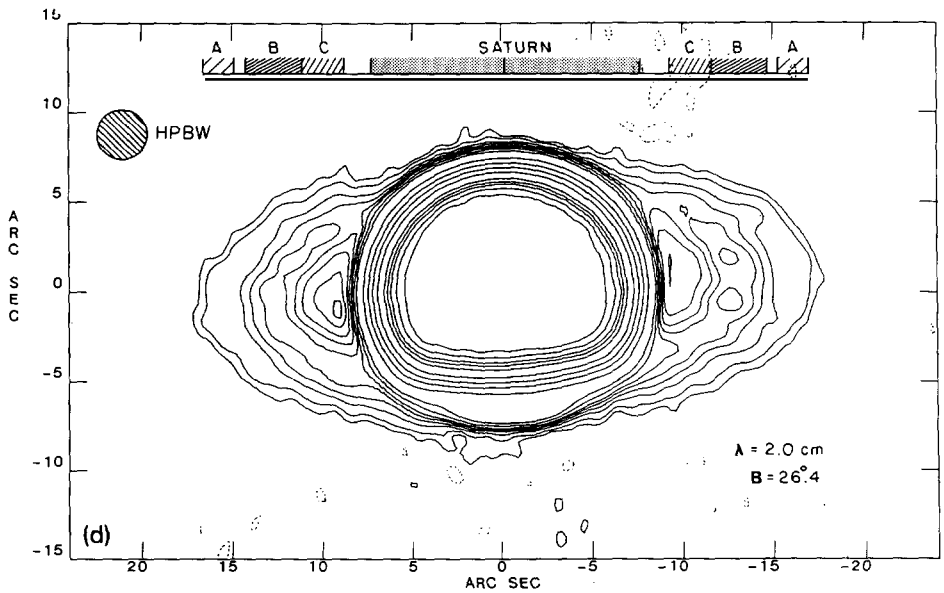

Fig. 5. Panel B. Radio images of Saturn; contour maps (c) and (d).

model calculation after Briggs and Sackett [1989] for a solar composition atmosphere (dashed curve), and an atmosphere in which H_2O and CH_4 are enhanced by a factor of 5, NH_3 gas by a factor of 3, and H_2S gas by a factor of 11 in the planet's deep atmosphere (solid line). The NH_3 mixing ratio decreases with altitude due primarily to the formation of an NH_4SH cloud at 3–5 bar level. The data at short centimeter wavelengths imply a larger decrease in NH_3 gas than suggested by Briggs and Sackett, which can be obtained by increasing the H_2S abundance to 12 or 13 times the solar value. The enhancement of NH_3 gas in the deep atmosphere is necessary to reproduce the long wavelength range of Saturn's spectrum. In the past, Klein et al. [1978] suggested that the low brightness temperature at wavelengths longwards of about 6 cm was due to the presence of a water cloud at levels in the atmosphere below about 270 K. However, an enhancement in the water mixing ratio changes the spectrum at 6–20 cm only slightly if the atmosphere is in thermo-chemical equilibrium.

The first radio image of the planet was obtained by Schloerb et al. [1979] at a wavelength of 3.7 cm. The data were obtained with the interferometer of the Owens Valley Radio Observatory using thirteen different baselines. The resolution was $8 \times 15''$. After subtraction of a uniform disk from the map, the contribution from the rings was visible as a positive signature at either side of the planet, and negative where the rings obscured part of the planet's radio emission. The first VLA images were published by de Pater and Dickel [1982]. In later years, images with a better quality were obtained (e.g., de Pater and Dickel [1983], de Pater [1985], Grossman et al. [1989], de Pater and Dickel [1989]). Figure 5 shows a few of the VLA images [de Pater and Dickel 1989] at 2 and 6 cm, observed at different ring inclination angles. Panel A displays radio photographs, panel B contour maps. The resolution is 1.5″, and the ring inclination angle $B = 12.5°$ and $\sim 26°$ for the 2 cm images, and 5.8° and 20° for the 6 cm images. The more recent images, at $B = 20°$ and 26°, clearly show the A and B rings separately; the Cassini Division can be distinguished as well. At 2 cm, the planetary disk shows no structure, other than that the planet seems less limb darkened in the north–south direction than expected for a uniform atmosphere. At 6 cm, however, there is a clear bright band across the planet at approximately 30° latitude.

Figure 6 shows meridional scans through several images at 6 cm, taken in different years: August 1981, January 1982, January 1984 and June 1986 respectively. The absorption effect by the rings differs from year to year, due to the varying ring inclination angle (and, to a smaller extent, the resolution of the beam). The planetocentric latitude of 30° is indicated by an arrow, and the bright band in the atmosphere appears to have moved southward over the years. Also, the intensity of this band might have changed, as well as the amount of limb darkening towards the pole. Higher resolution images suggest the presence of a second, much weaker, bright band near the equator, and one in the southern hemisphere.

Model atmosphere calculations show that the difference in brightness temperature between the bright band and the rest of the planet can be explained by a difference in the ammonia mixing ratio at levels in the atmosphere where $P \sim 1$–5 bar. Grossman et al. [1989] suggest a 30% decrease in the NH_3 mixing ratio in the bright band. However, with a three-times solar mixing ratio of NH_3 gas at $P \gtrsim 5$ bar, the ammonia abundance in the bright band must be decreased by nearly 50% at $P < 5$ bar. Such an effect would also be visible at 2 cm wavelength. De Pater and Dickel [1989] suggest that the global NH_3 abundance in the upper atmosphere is about 5×10^{-5}. The low abundance extends to deeper levels in Saturn's atmosphere in the bright band, than at other positions: down to 4–4.5 bar in the bright band, and to 2.5–3 bar everywhere else. This implies that the NH_4SH cloud layer forms at a deeper level in the atmosphere in the bright band, than at other latitudes. In addition, the vertical extent of the cloud layer is about 0.5 bar in both regions. Note that this is opposite to what we saw on Jupiter.

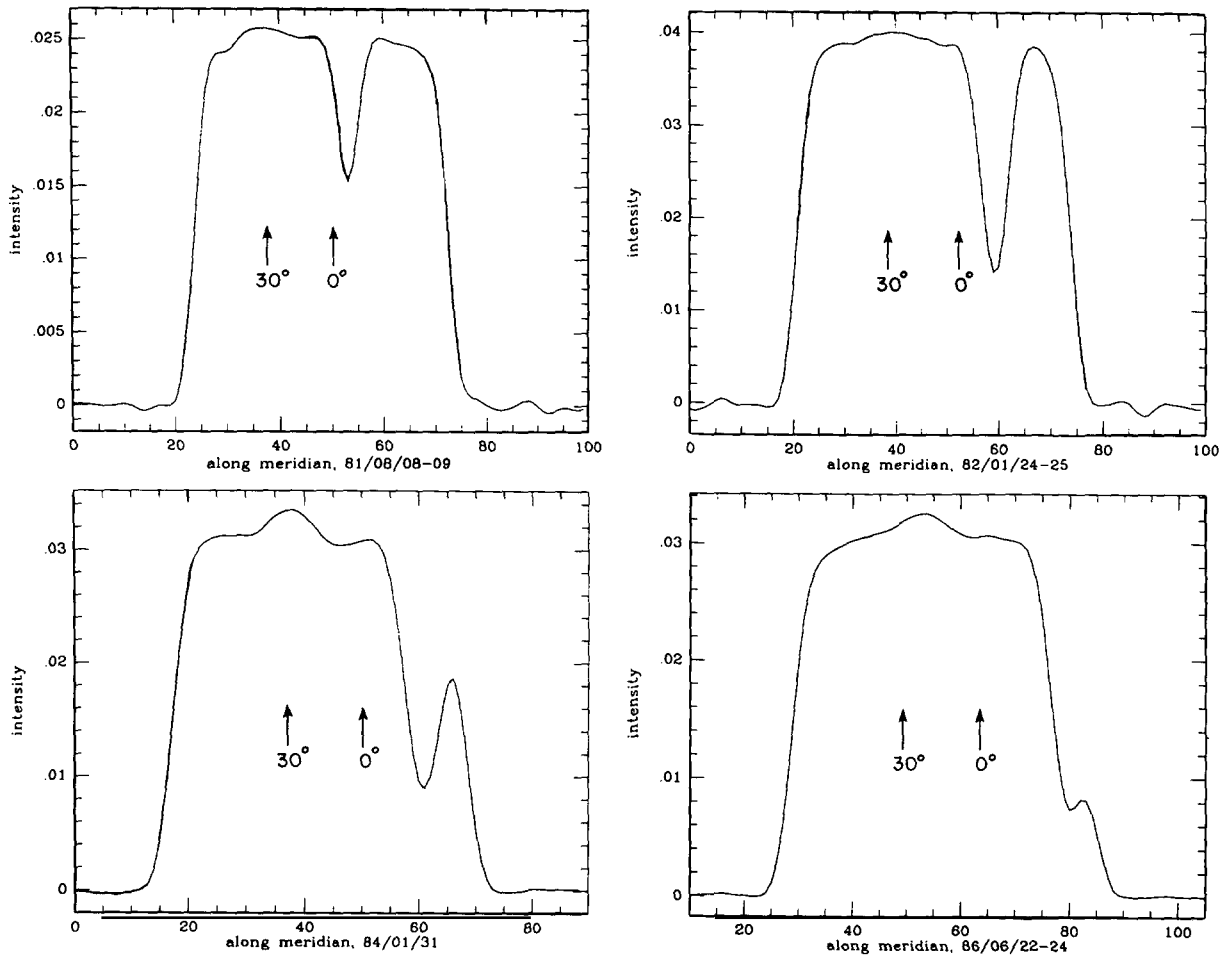

Fig. 6. Meridional scans through 6 cm images of Saturn. The data were taken in August 1981, January 1982, January 1984, and June 1986, respectively. The planetocentric latitudes of 0° and 30° are indicated by arrows.

From limb darkening curves it appears that in both Jupiter's and Saturn's atmospheres the ammonia abundance above the NH_4SH cloud deck decreases by approximately a factor of 2 towards the poles, while the underlying higher ammonia abundance starts at higher levels in the atmosphere near the polar regions. Since the ammonia abundance above the NH_4SH cloud layer is largely determined by the abundance of H_2S, the latter may increase somewhat from the equator to the pole. Also the altitude at which the NH_4SH cloud forms apparently varies with latitude. The reaction $NH_3 + H_2S \rightarrow NH_4SH$ is heterogeneous, so it requires the presence of solid surfaces, as, e.g., aerosols. Hence the variation in the NH_3 abundance with latitude and altitude depends upon the H_2S abundance as well as the aerosol distribution, which is probably tied in with the dynamics on the planet.

Far-infrared (IRIS) observations obtained with the Voyager spacecraft probe pressure levels of ~0.3–0.7 bar. A warm band is visible at mid-latitudes, similar to the band seen at radio wavelengths [Bezard et al., 1984]. However, if, at these pressure levels, this region is hot due to an enhancement in the physical temperature of this band, the hot band should show up in the radio images at 2 cm. Likely,

as suggested by the authors, the feature seen at infrared wavelengths is due to a latitudinal variation in cloud opacity. A thinner NH_3-ice cloud at mid-latitudes would imply a region of downwelling, which is consistent with the interpretation of an altitude variation with latitude of the NH_4SH clouds derived from the radio data.

1.4.2. Rings

As mentioned above, radio interferometric observations were used to extract information on the microwave properties of Saturn's rings. Observations at different wavelengths and polarizations can be used to determine the composition and sizes of the ring particles, through their scattering characteristics. Cuzzi et al. [1980] present detailed theoretical models of the brightness of Saturn's rings at microwave wavelengths, including both intrinsic ring emission and diffuse scattering of the planetary emission by the rings.

Schloerb et al. [1980] show that the effective normal optical depth of the A and B rings decreases with decreasing ring inclination angle, such as expected for the classical A and B rings, with a clear open gap, the Cassini Division, in between. Table 1 lists the optical depths as well as the ring brightness temperatures from all observations reported to date (after Esposito et al. [1984]). Figure 7 shows a graph of the data points of the effective optical depth, τ_{eff}, with superimposed a theoretical calculation of τ_{eff} (after Schloerb et al. [1980], not a fit to the data!),

$$\exp(-\tau_{\text{eff}}/\sin|B|) = f_{\text{A}} \exp(-\tau_{\text{A}}/\sin|B|) + f_{\text{B}} \exp(-\tau_{\text{B}}/\sin|B|) + f_{\text{CD}}\,, \tag{2}$$

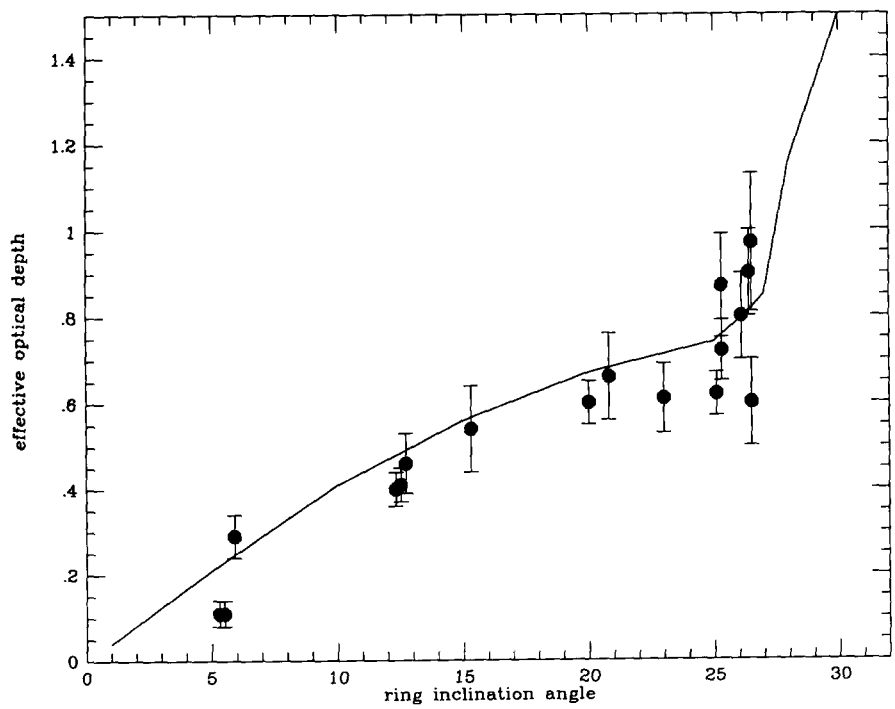

Fig. 7. A graph of the effective optical depth of the combined A and B rings as a function of ring inclination angle (after Schloerb et al. [1980]). The solid line is a prediction for the effective optical depth, if $\tau_{\text{A}} = 0.7$, and $\tau_{\text{B}} = 1.5$.

Table 1
Optical depth for A and B rings, as derived from observations at different ring inclination angles. Note that all values from de Pater and Dickel [1989] are still preliminary

Wavelength (cm)	B (deg.)	τ_{eff} A, B	$T(A+B)/T(S)$ (%)	reference[a]
0.10	22.0		24.0 ± 5.0	[Werner et al. 1978; Esp]
0.14	26.6		50.0 ± 17.0	[Rather et al. 1974; Esp]
0.14	26.4		36.0 ± 8.0	[Courtin et al. 1977; Esp]
0.17	20.1		33.0 ± 6.0	[Rowan-Robinson et al. 1978; Esp]
0.21	26.4		15.7 ± 8.6	[Ulich 1974; Esp]
0.27	23.0	0.61 ± 0.08	12.0 ± 2.0	[Dowling et al. 1987]
0.33	0–26		11.5 ± 5.1	[Epstein et al. 1980]
0.34	0–26		10.8 ± 2.6	[Epstein et al. 1984]
0.35	26.5		5.3 ± 4.7	[Ulich 1974; Esp]
0.86	21–25		8.8 ± 1.4	[Janssen and Olsen 1977]
1.30	−15.3	0.54 ± 0.10	4.4 ± 0.8	[Schloerb et al. 1980]
1.33	−5.4	<0.06		[de Pater and Dickel 1982]
1.34	12.5	0.46 ± 0.07	7.5 ± 1.0	[de Pater and Dickel in preparation]
1.99	−5.4	0.11 ± 0.03		[de Pater and Dickel 1982]
2.0	12.5	0.41 ± 0.04	5.7 ± 0.8	[de Pater and Dickel in preparation]
2.0	25.3	0.87 ± 0.12	4.4 ± 0.5	[Grossman et al. 1989]
2.0	26.4	0.9 ± 0.1	4.6 ± 0.2	[de Pater and Dickel in preparation]
3.71	−20.8	0.66 ± 0.10	4.2 ± 0.7	[Schloerb et al. 1980]
3.71	−26.1	0.8 ± 0.1	5.2 ± 1.7	[Cuzzi and Dent 1975; and Schloerb 1978]
3.71	−26.5	0.97 ± 0.16	3.1 ± 0.7	[Schloerb et al. 1980]
3.71	25.6		6.5 ± 1.2	[Briggs 1974; Esp]
6.0	−26.5	0.6 ± 0.1	3.4 ± 0.6	[Jaffe 1977; Schloerb, 1978]
6.14	−5.4	0.11 ± 0.03		[de Pater and Dickel 1982]
6.14	5.9	0.29 ± 0.05	3.8 ± 0.5	[de Pater and Dickel in preparation]
6.14	12.5	0.40 ± 0.04	4.3 ± 0.5	[de Pater and Dickel in preparation]
6.17	20.0	0.60 ± 0.05	4.4 ± 0.2	[de Pater and Dickel in preparation]
6.17	25.1	0.62 ± 0.05	4.7 ± 0.2	[de Pater and Dickel in preparation]
6.17	25.3	0.72 ± 0.07	3.6 ± 0.2	[Grossman et al. 1989]
21.0	25.2		2.7 ± 1.4	[Briggs 1974; Esp]

[a] Esp stands for Esposito et al. [1984].

with f_A, f_B, and f_{CD} the fraction of the obscured region of the planet blocked by the A and B rings, and the Cassini Division respectively. The latter division was assumed to be entirely transparent at radio wavelengths. The optical depth in the A-ring was taken to be 0.7, and in the B-ring as 1.5. It is clear that the trend in the observed effective optical depth follows the theoretical prediction. In this figure no differentiation is made between points at different wavelengths, although Cuzzi et al. [1980] show that the optical depth of the rings may decrease with wavelength if the rings are wide open. They used this fact to constrain the size of the ring particles to be primarily less than a meter.

Schloerb et al. [1980] pointed out that at small ring inclination angles the effective optical depth approaches the optical depth of the least optically thick region. With a transparent Cassini Division, or other clear open gaps in the rings, this will be zero as shown on the graph. Cuzzi et al. [1980] show that the ring particles scatter preferentially in the forward direction. High resolution VLA observations of the ring system, such as those presented in fig. 5 confirm this suggestion [Grossman et al. 1989; de Pater and Dickel 1989], since the far side of the ring is usually weaker than the near side. The fact that the particles scatter preferentially in the forward direction will also cause the effective ring optical depth to decrease with decreasing ring inclination angle.

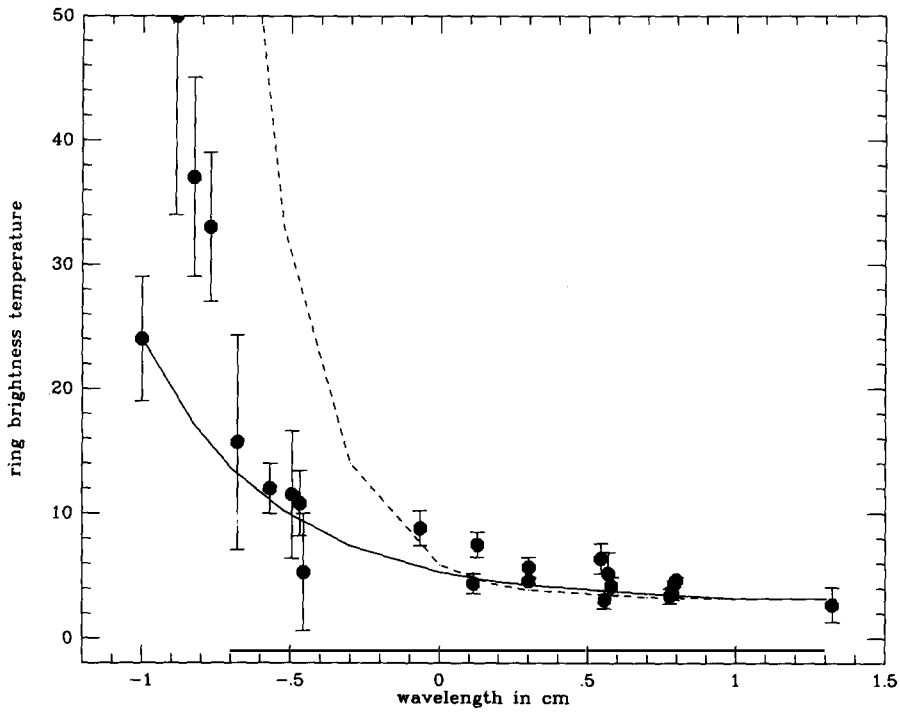

Fig. 8. The brightness temperature for the combined A and B rings as a function of wavelength (after Cuzzi et al. [1980]). The dashed line shows a thermal spectrum with a λ^{-2} dependence; the solid line shows a spectrum with a λ^{-1} dependence.

Thermal radiation from the ring particles has been observed at wavelengths between ~10 μm and ~1 cm. Somewhere between 100 μm and 1 mm wavelength, the ring brightness temperature drops below the black body behavior, and longwards of 1 cm wavelength the rings behave nearly like a perfect reflecting surface. Esposito et al. [1984] show that the brightness temperature rises approximately as $\sim 1/\lambda$ shortwards of 1 cm, as expected from an optically thick slab of particles which are nearly conservative scatterers [Cuzzi et al. 1980]. Figure 8 shows the data together with curves $\sim\lambda^{-1}$ and λ^{-2} (after Esposito et al. [1984]). The low intrinsic brightness temperature of the rings at centimeter wavelengths, together with the observed perfect reflector behavior hints at an icy composition of the particles. In addition, the ring particles cannot be primarily smaller than ~1 cm, independent of their precise composition [Cuzzi et al. 1980].

The high resolution images better constrain the optical depth and ring brightness temperature of the individual A, B, and C rings. Rather than making model fits to the UV data, the images can be used directly to determine the ring properties. Grossman et al. [1989] show the optical depth and ring brightness temperature for the three rings and Cassini Division separately, as determined directly from the images. They conclude from their measurements that the A and C rings contain many particles in the size range 0.6–2.0 cm, while the B ring contains a greater population of large particles.

1.5. Uranus

The angular diameter of Uranus subtends an angle of less than 4″ as seen from the earth; therefore, until the VLA could be used to image the planet, most radio observations were of the unresolved disk.

The Planetary Radio Astronomy group at the Jet Propulsion Laboratory [Klein 1984] assembled a catalogue of all radio data of Uranus, and recalibrated older data points so all temperatures are on the same flux density scale. Their catalogue was published in a review paper on Uranus by Gulkis and de Pater [1984]; since this publication more observations have been made (see de Pater and Gulkis [1988], Berge et al. [1988]), which are included in the spectrum shown below.

A spectrum of disk-averaged brightness temperatures of Uranus is shown in fig. 9. As was first pointed out by Gulkis et al. [1978], Uranus' brightness temperature is too high to be matched by a solar composition atmosphere, as indicated by the dashed line in fig. 9. The most up to date model calculations made to date are by de Pater et al. [1989] and are also shown in fig. 9; the dotted curve is a model for an atmosphere in thermo-chemical equilibrium in which both the H_2S and H_2O abundances are enhanced by a factor 500 compared to the solar S and O values respectively, and NH_3 by a factor of 15 compared to the solar N value (note: CH_4 was always assumed to be 30 times enriched above the solar C value to match the observed 2% mixing ratio in the upper troposphere [Lindal et al. 1987]). The solid line is for the same model but with NH_4SH "supersaturated" at $P < 30$ bar ($T < 240$ K), where the NH_3 abundance is 3.5×10^{-7}. In the latter model no condensation of NH_4SH occurs, even though the product of the partial pressures of H_2S and NH_3 exceeds the equilibrium constant at these pressure levels. This effectively "forced" the ammonia abundance to be constant over a large range in altitude, a feature which is necessary to match the steep part of the planet's radio spectrum at wavelengths between 0.3 and 6 cm.

A similar result can be obtained by fast vertical mixing in the atmosphere; however, since the eddy diffusion coefficient should be unrealistically large for this process to be effective, the authors dismissed

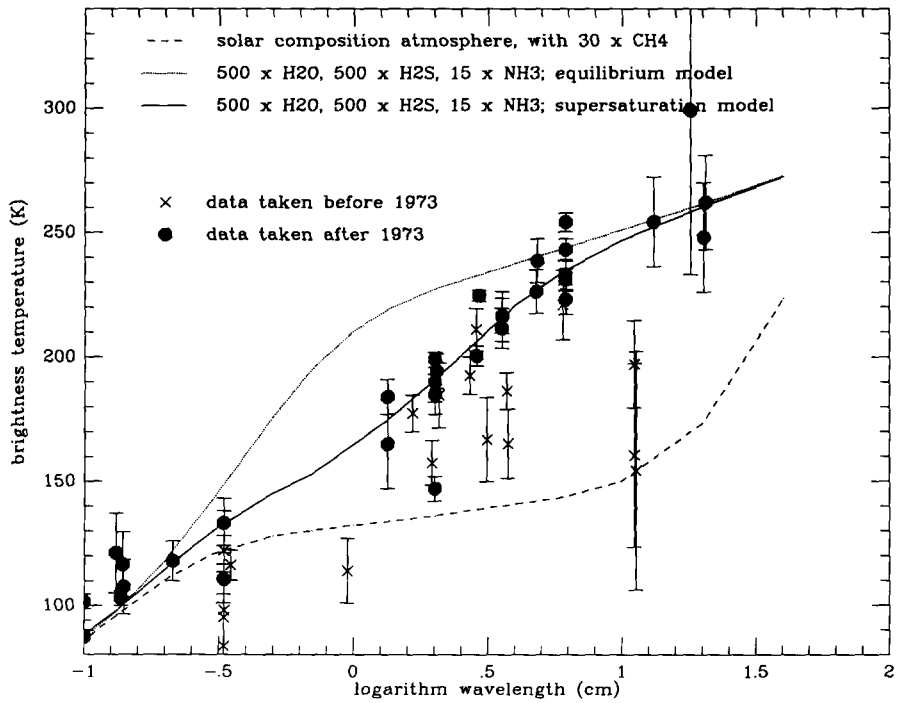

Fig. 9. Radio spectrum of Uranus, with superimposed various model atmosphere calculations from de Pater et al. [1989], as indicated in the figure. See text for further explanations.

the mixing model. In addition to the supersaturation model, the H_2S concentration needs to be large (larger than 100 times the solar S value), to force the formation of the NH_4SH cloud to occur deep in the atmosphere, so ammonia gas gets depleted significantly at large depths in the atmosphere. The authors also considered the possibility of a subsolar NH_3 abundance throughout the atmosphere, but dismissed this case; the synthetic spectra did not fit the data as well as those in which ammonia gas was equal to or enhanced above the solar value. In addition, if NH_3 gas is subsolar, the nitrogen should be present in the form of N_2, unless N itself is deficient. However, the upper limit to the detection of N_2 by the Voyager UVS experiment is on the order of one part per billion at the 1 mbar level. This implies that most of the nitrogen in Uranus' atmosphere must be in the form of NH_3, not N_2. Hence, the authors concluded the abundances of the various constituents to be: S > 100 × solar; N > 1–10 × solar; O > solar; S/N ratio > 3 if $H_2O \gtrsim 100 \times$ solar, or >5, if $H_2O \lesssim 100 \times$ solar. Unfortunately, they could not place a tighter constraint on the water abundance.

1.5.1. Variability

In 1978, Klein and Turegano [1978] noted an increase in Uranus' disk-averaged brightness temperature at a wavelength of 3 cm. Gulkis et al. [1983] discussed the time variability in detail; some aspects of it were improved by Gulkis and de Pater [1984]. As shown in fig. 9, data points taken before 1973 generally indicated a colder planet than data taken after 1973. When correcting for the shape of the spectrum between 2 and 6 cm one can make a graph of the data points in this wavelength range as a function of time. Figure 10 shows such a graph (open circles: data at 6 cm; dots: data at $\lambda < 6$ cm),

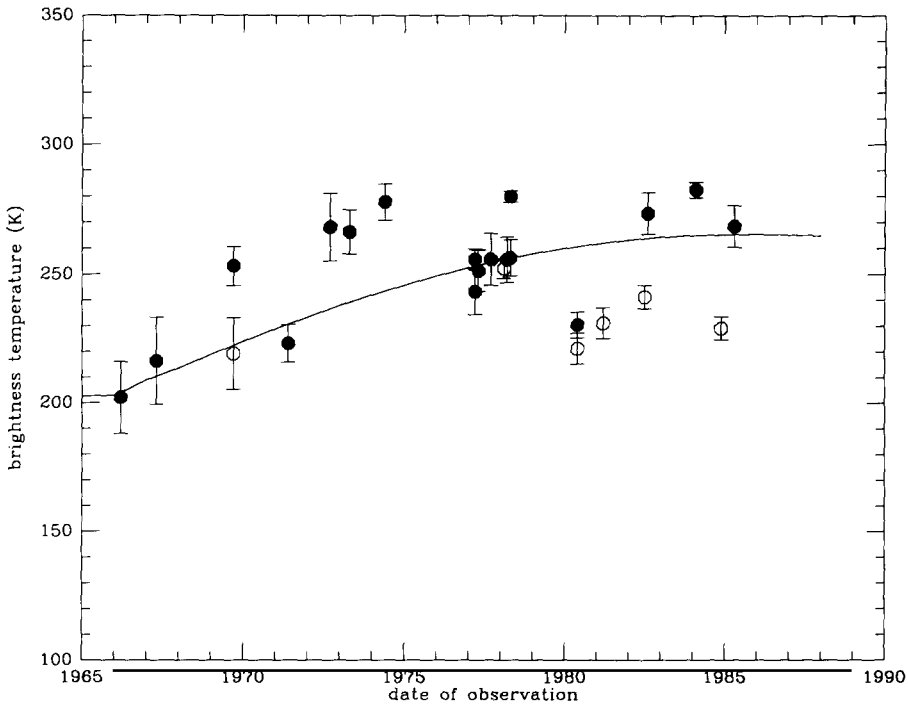

Fig. 10. Uranus' disk-averaged radio brightness temperature as a function of time. The open circles are data taken at 6 cm; the filled circles are for data taken at $1.3 < \lambda < 5$ cm (after Gulkis and de Pater [1984]). The solid line is the predicted behavior if Uranus' pole is much warmer than the equator (see text).

where the data were corrected for the slope in the spectrum according to [Gulkis and de Pater 1984]

$$T_C = T_D - 76 \ln(\lambda) + 136.2 , \tag{3}$$

where T_C is the brightness temperature corrected for the slope, T_D the observed disk-averaged brightness temperature and λ the wavelength in cm. Superimposed on the data points is a model, with a permanent brightness temperature distribution on the disk as [Gulkis and de Pater 1984]

$$T = T_0 + 0.66(T_p - T_e)\cos(\theta) , \tag{4}$$

with T_p and T_e the temperatures at the pole and equator respectively, and θ the colatitude on the planet. With a temperature gradient of 100 K, and $T_0 = 200$ K, this variation roughly corresponds to the temperature gradient between the pole and equator as seen on a 6 cm VLA image [Gulkis and de Pater 1984] (see below). The data show the same overall trend as the model, although significant deviations from the model are seen. In addition, the variability is most significant at wavelengths shortwards of 6 cm.

1.5.2. Latitudinal brightness distribution

Briggs and Andrew [1980] were the first to notice a large temperature gradient on Uranus between the equator and the pole, at a wavelength of 6 cm. Their conclusions were based upon visibility data obtained with an interferometer. The first radio images were published by Jaffe et al. [1984]. At 2 cm the image showed a symmetric disk as expected for a uniform gaseous planet, with the brightest point at the subearth point, and limb darkened towards the limb. At a wavelength of 6 cm, however, the planet appeared asymmetric in that it showed the brightest point on the planet to be near the pole rather than the subsolar point.

Since that time Uranus has been imaged regularly at 2 and 6 cm [de Pater and Gulkis 1988; Berge et al. 1988]. Examples of images are shown in fig. 11: a 6 cm image from 1982, and a 2 cm image from 1984 (from de Pater and Gulkis [1988]). The asymmetry at 6 cm is always present, although the detailed latitudinal distribution of the brightness temperature varied significantly over the years. This is shown schematically for two years on fig. 12 (from de Pater et al. [1989]). An analysis of the 2 cm data of Berge et al. [1988] by Hofstadter and Muhleman [1989] shows two rather than 3–4 zonal bands, one between 0° and ~45°, and a warmer band between ~45° and the pole. In addition to time variations in the latitudinal structure, the position of the brightest point on the disk at the 2 cm images appeared to move from the subsolar point to a point closer to the pole between the years 1980 and 1984–1985.

Even though the detailed latitudinal structure changes drastically on timescales of about a year (or shorter), the general zonal distribution always seems present; a hot polar region at latitudes larger than 70°: 270–280 K at 6 cm, and 240–250 K at 2 cm; a cold equatorial band below roughly 30–40°: 220 K at 6 cm, and 160–170 K at 2 cm; and up to two bands at mid-latitudes: ~250 K at 6 cm, and 200–220 K at 2 cm. These zonal variations can be explained in terms of a latitudinal variation in the ammonia abundance. Using the "supersaturation" model of de Pater al. [1989] the NH_3 abundance is 2×10^{-6} at $T < 240$ K in the equatorial region, $(1–2) \times 10^{-7}$ at $T < 220$ K at mid-latitudes and 10^{-7} down to 280 K in the polar region. The gaseous ammonia abundance will follow the saturated vapor curve at $T \lesssim 145$ K, when NH_3 gas condenses out.

These abundances hint at a general upwelling of gas at mid-latitudes, with subsidence in the equatorial region (and at higher latitudes). This atmospheric circulation supports the meridional flow as

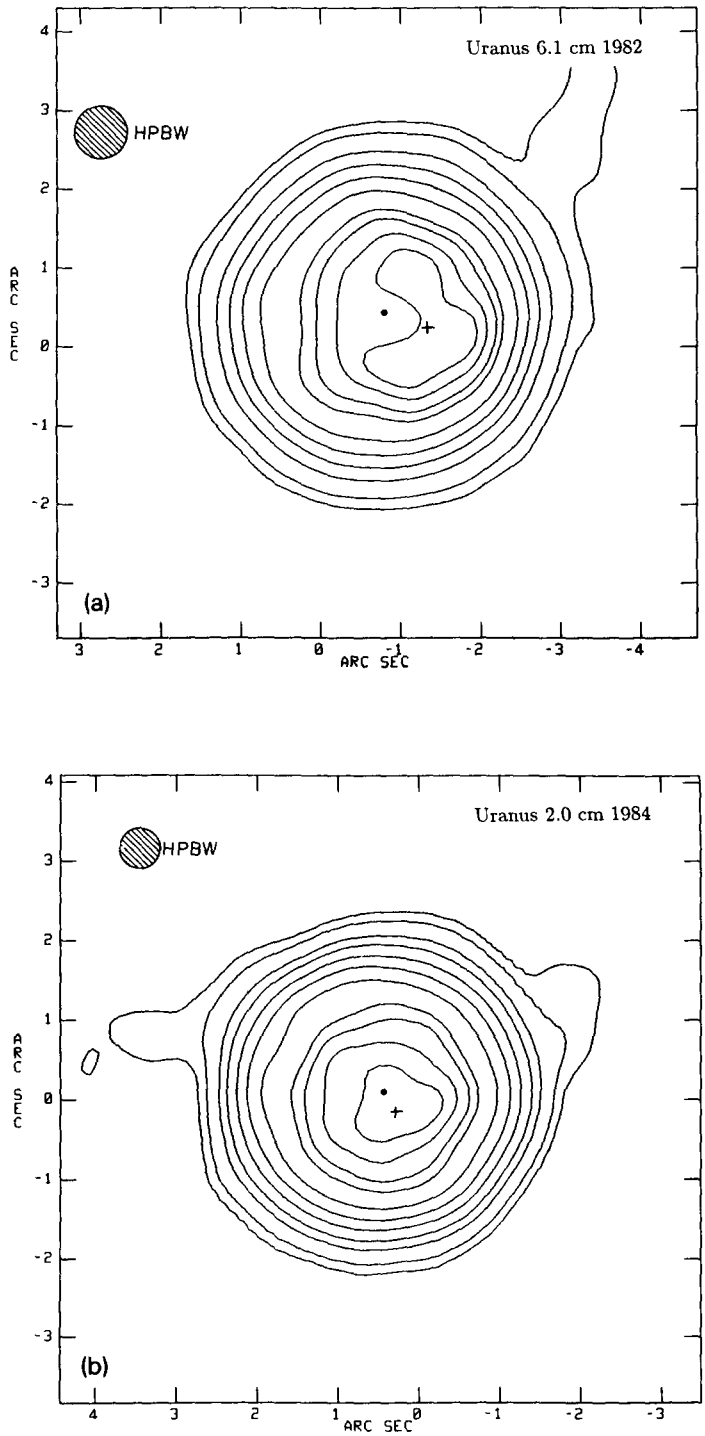

Fig. 11. Radio images of Uranus at (a) 6 and (b) 2 cm from de Pater and Gulkis [1988]. The cross indicates the position of the pole, the dot of the subsolar point. The resolution of the images is 0.65″ for the 6 cm image, and 0.5″ for the 2 cm image. The contour values are: (a) at 6 cm: 14, 28, 69, 110, 151, 193, 234, 248, 261, and 270 K; (b) at 2 cm: 11, 22, 55, 88, 121, 154, 187, 198, 209, and 216 K.

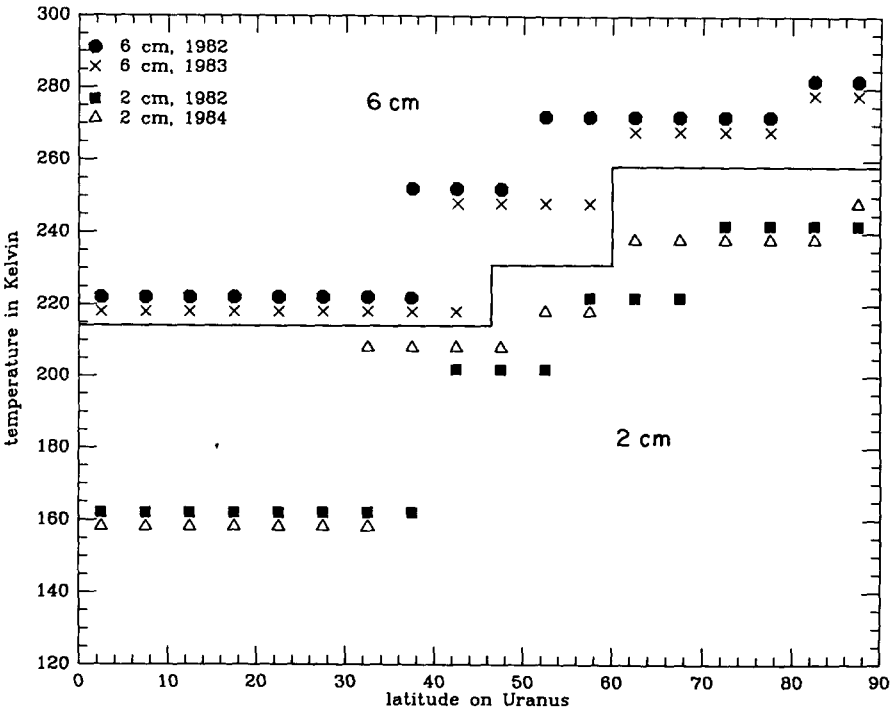

Fig. 12. Uranus's radio brightness temperature as a function of "latitude" with respect to the point of symmetry on the planet (taken as 90°). Distributions at 2 and 6 cm are shown, for two different years (from de Pater et al. [1989]).

derived from Voyager observations by Flasar et al. [1987]. It further causes condensation nuclei to be present at higher altitudes at mid-latitudes than in the equatorial region. Since these nuclei are necessary for the reaction $NH_3 + H_2S \rightarrow NH_4SH$ to take place, it supports the idea that the formation of NH_4SH is confined to deeper levels in the atmosphere in the equatorial region than at higher latitudes. The low ammonia abundance in the polar regions, down to levels as deep as 280 K cannot be explained in terms of the "supersaturation" model; the authors suggest the existence of strong downdrafts of dry air (air from which the NH_3 has been removed by condensation) to a depth of at least 280 K.

1.6. Neptune

The first radio astronomical detection of Neptune was made in 1966 by Kellermann and Pauliny-Toth [1966], at a wavelength of 1.9 cm. Despite the lapse of time since this measurement, the spectrum of the planet still is poorly defined. Obviously, this is mainly due to the faintness of this distant object, causing many problems due to confusion in the signals received by single antennas. The confusion is minimized when the source is observed with an interferometer. De Pater and Richmond [1989] published a paper on VLA observations of Neptune, and refined the planet's spectrum. Their spectrum is shown in fig. 13, with the VLA data points indicated by filled circles, and others by crosses. It is clear that Neptune, like Uranus, is too warm at centimeter wavelengths for a solar composition atmosphere (dashed line on fig. 13). A straight model atmosphere calculation (after de Pater and Massie [1985]) gives a best fit to the

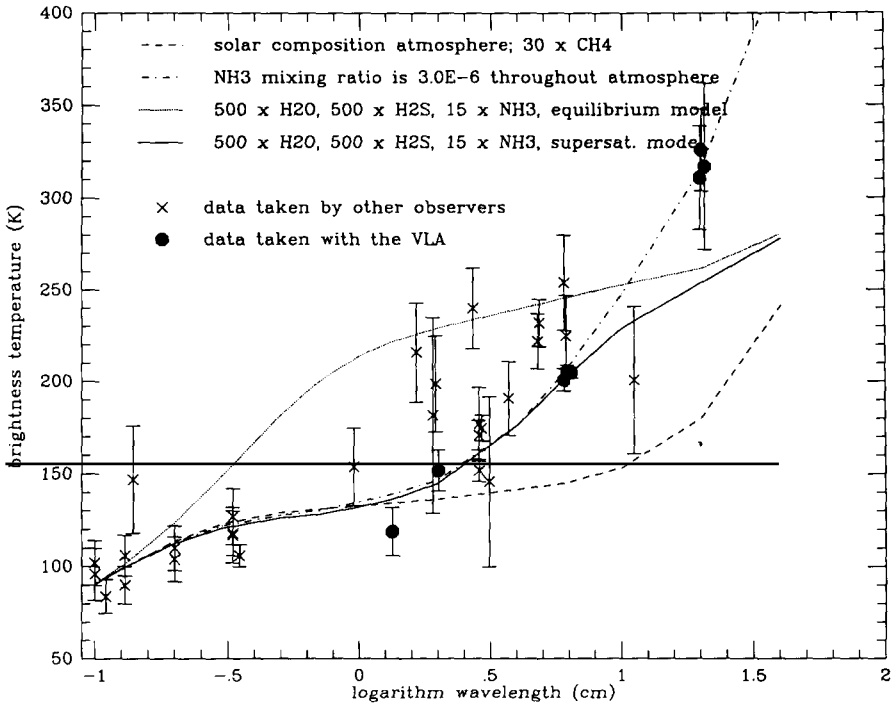

Fig. 13. Radio spectrum of Neptune (after de Pater and Romani [1989]). Superimposed are various model atmosphere calculations as indicated in the figure.

data, if the NH_3 abundance is equal to 3×10^{-6} throughout the atmosphere (short-dash–long-dash curve on fig. 13). Model atmosphere calculations after Romani et al. [1989] are presented by the dotted and solid lines respectively; the dotted line is a calculation in thermo-chemical equilibrium, for a planet with the same composition as Uranus: $30 \times CH_4$, $500 \times H_2O$, $500 \times H_2S$, and $15 \times NH_3$, compared to the solar C, O, S, and N values. The solid line is the same calculation for an atmosphere in which the NH_4SH cloud was assumed to be supersaturated at layers where $T < 240$ K. Although the latter curve fits the data shortward of ~10 cm reasonably well, neither of the solid curves can match the rather high brightness temperature of 318 ± 16 K at 20 cm. These data can only be matched if NH_3 gas is less than solar throughout the atmosphere by a factor of about 50 compared to the solar N value, as shown by the dashed curve. Based upon planetary formation theories and a comparison with nearby Uranus, a depletion of NH_3 gas by nearly two orders of magnitude compared to the solar value seems highly unlikely.

Synchrotron radiation?

In analogy with Jupiter, de Pater and Richmond [1989] suggested the excess emission at 20 cm, 0.4 ± 0.13 mJy, to be due to synchrotron radiation emitted by energetic electrons in a Neptunian magnetic field. De Pater and Goertz [1989] performed some calculations on the inward diffusion of energetic electrons, and suggested that Neptune's surface magnetic field strength at the equator will be about 0.5 G if the particle distribution is similar to that in Jupiter's radiation belts. The field strength has been confirmed by the recent Voyager flyby, but no energetic particles were observed.

1.7. Discussion and conclusions

The radio spectra and resolved images of the four giant planets were discussed above. All four planets show a sub-solar ammonia mixing ratio in the upper atmosphere, and an enhancement in the lower part. On Jupiter and Saturn NH_3 gas is depleted by a factor of about 5 at $P \lesssim 1$ bar (Jupiter) – 3.5 bar (Saturn), and enhanced by 1.5 on Jupiter, and 3–4 on Saturn at deeper levels in their atmospheres. Bright bands across the two planetary disks imply a latitudinal variation in the precise ammonia abundance. Uranus and Neptune show a depletion in NH_3 gas of nearly two orders of magnitude over a large altitude range in the atmosphere. The gas is probably enhanced by an order of magnitude or more at deeper levels. In addition, Uranus shows a large pole-to-equator gradient in the ammonia abundance.

The loss of NH_3 gas in the atmospheres of all four planets is most likely due to the formation of NH_4SH, which in thermo-chemical equilibrium calculations is expected to form at the pressure levels where the decrease in the ammonia gas abundance is observed. To obtain a large enough loss in ammonia gas at the right pressure levels, the H_2S abundance in Jupiter and Saturn needs to be enhanced by a factor of 6–7 and 10–15 respectively, compared to the solar S value, and by $\gtrsim$100 on Uranus and Neptune. In addition, the S/N ratio on the outer two planets needs to exceed 3, if the H_2O abundance is larger than a hundred times the solar O value, or 5 if the H_2O abundance is less than a hundred times the solar value.

Due to the variations in enrichment factors for the heavy elements in all four planets, the cloud structure between the planets is rather different. On Jupiter we do not expect to find a solution cloud; on Saturn it is small (base at ~20 bar level), but on Uranus and Neptune it is very extensive (base near 2000 bar level). On all four planets water-ice will form at a temperature of about 270 K. At higher altitudes, the NH_4SH cloud layer will form. The base level of the cloud is roughly near 210–230 K (2–5 bar level) on Jupiter and Saturn, and 280 K (~100 bar level) on Uranus and Neptune. On Jupiter and Saturn, no H_2S gas will be left above this cloud layer. At temperatures of 140–150 K NH_3 gas will freeze out and form ammonia-ice. This is the cloud layer "visible" at optical wavelengths. On Uranus and Neptune there is a lot of H_2S gas present above the NH_4SH cloud layer. This gas will condense out at a temperature of about 170–180 K (~10–15 bar). Since NH_3 gas is supersaturated above the NH_4SH cloud layer, we find a small ammonia-ice cloud near 120 K (3–4 bar level). On the latter two planets the temperature gets also cold enough for CH_4 gas to freeze out, at about 80 K (~1 bar level). The latter cloud deck is "seen" at visible wavelengths.

Table 2 contains a summary of the abundances of various heavy elements in the giant planets (after Pollack and Bodenheimer [1989] supplemented with the values presented in this paper). These abundances should be compared with current models on planetary formation. Pollack and Bodenheimer [1989] favor the "core-instability" model for planetary formation in which the core of the giant planets is formed first by solid body accretion, similar to the formation of the terrestrial planets. When the mass reaches a critical value, gas accretion from the surrounding proto-planetary nebula becomes very rapid. This model accounts for the fact that the total mass made up of "heavy" elements (elements with atomic masses larger than H_2 and He) is similar for the four giant planets. For Jupiter, Saturn and Uranus/Neptune, this mass is roughly 5, 25 and 300 times larger, respectively, than would be expected from solar elemental abundances. Furthermore, models of the interior structure of the planets show that the envelopes of the planets also contain large amounts of heavy elements. This can be accounted for in the "core-instability" hypothesis by the fact that late accreting planetesimals have an increasing difficulty to penetrate through the denser and denser envelope.

Table 2
Composition of the atmospheres of the giant planets (after Pollack and Bodenheimer [1988], supplemented with other values)

Element	Abundance with respect to the solar volume mixing ratio				reference
	Jupiter	Saturn	Uranus	Neptune	
C	2.3 ± 0.2	5.1 ± 2.3	35 ± 15	40 ± 20	[Courtin et al. 1984; Lindal et al. 1987; Orton et al. 1987;
P	$>1.4 \pm 0.4$	$>2.8 \pm 1.6$			[Courtin et al. 1984]
S	6–7	10–15	>100	>100	[de Pater 1986; de Pater and Dickel in preparation; Briggs and Sackett 1989; de Pater et al. 1989; Romani et al. 1989]
O	>1	>1	>1	>1	[Carlson et al. 1988; de Pater and Massie 1985; de Pater et al. 1989; Romani et al. 1989]
N	1.5 ± 0.2	3.5 ± 1	$1 < N < 100$		[de Pater, 1986; de Pater and Dickel in preparation; Briggs and Sackett 1989; de Pater et al. 1989; Romani et al. 1989]
He	0.65 ± 0.15	0.2 ± 0.15	1 ± 0.15		[Conrath et al. 1987]

Based upon the observed methane abundances in the giant planets' atmospheres (2.3, 5.1, 30–40 times the solar value on Jupiter, Saturn, Uranus/Neptune respectively), Pollack and Bodenheimer [1989] (and references therein) estimate that about 10% of the carbon in the outer solar nebula was in the condensed phase during the epoch of planetary formation. Rocky and refractory elements, like Mg, Si, P, S, and water were entirely in the solid phase, although part of the O was present in the form of mineral oxides and CO gas. The regular satellites of the giant planets are all made of rock and ice, with a mean rock/ice ratio of 55/45 by mass. However, since water is somewhat easier to dissolve in the envelopes of the forming giant planets, the authors predict that the envelopes of the planets contain somewhat more water than rock by mass. So they expect the O/S ratio to be slightly larger than the solar value. Like carbon, nitrogen is expected to have been present in both the gas (e.g., N_2) and solid phase. Since the N/C ratio was found to be subsolar in meteorites and comets, Pollack and Bodenheimer predict the N/C ratio in the envelopes of the giant planets to also be subsolar by a factor of about 2. Hence, the abundances for the various elements as given in table 2 tend to support Pollack and Bodenheimer's theory on planetary formation. The N/C ratio, wherever determined, is typically of the order of 0.5; the S/C ratio is of the order of 5 or larger; unfortunately, no constraints on the oxygen abundance are known, other than that H_2O is at least equal to the solar O value on all planets. Hence, the O/S ratio can indeed exceed unity as the formation theories predict.

The latitudinal variation in the brightness temperature on the various planets is most likely due to a latitudinal variation in the precise ammonia abundance, caused by latitudinal variations in the location of the ammonium hydrosulfide cloud in the atmosphere. Since this cloud only forms in the presence of solid surfaces, the location probably coincides with layers of aerosols. The location and abundance of the latter particles depend upon the origin of the aerosols, and the dynamics in the atmosphere. Our study implies that the conditions for the NH_4SH cloud differ from one planet to the next. On Jupiter, the vertical extent of the NH_4SH cloud is larger in the zones than the belts. The difference in latent

heat release between the clouds in the zones and belts may drive the zonal winds, and it causes upwelling of gas in the zones, and subsidence in the belts. On Saturn, the extent of the cloud in the bright band is similar to that in other regions, but it is confined to a deeper part in the atmosphere. This will cause differences in the temperature–pressure profile in the region between 2 and 5 bar, where the NH_4SH cloud forms. In this region we probably have rising gas in the bright band, and subsidence in the neighbouring regions. No clear correlation is seen with the wind profile measured with the Voyager spacecraft. On Uranus, we need a general increase in the NH_4SH cloud extent towards the pole. The distribution hints at a general upwelling of air at mid latitudes, with subsidence in the equatorial region and higher latitudes. In addition, there must be strong downdrafts of dry air in the polar region. Unfortunately, we do not yet have high resolution images of Neptune, on which we can resolve individual zonal bands. We expect the planet to have a zonal distribution of gases or winds as the other three planets.

2. Synchrotron radiation

2.1. Introduction

Synchrotron radiation is emitted by relativistic electrons gyrating around magnetic field lines. The radiation is beamed in the forward direction within a cone $1/\gamma$, with $\gamma = 2E$, and E the energy in MeV. The radiation is emitted over a wide range of frequencies, but shows a maximum at $0.29\nu_c$, with ν_c, the critical frequency in MHz, equal to

$$\nu_c = 16.08E^2B \tag{6}$$

with the energy E in MeV and the field strength B in G. For emission at 20 cm, we require $E^2B = 320$. If B is 0.5 G, the typical energy of electrons emitting at 20 cm is close to 25 MeV. At lower field strengths and/or higher observing frequencies, the typical energy increases. Hence we probe a different electron population when we observe at different frequencies. Further, since the magnetic field strength decreases with planetary distance r, approximately as r^{-3} for a dipole field, we also observe different electron distributions at different distances from the planet.

Synchrotron emission is generally polarized, and we express the observed quantities in terms of the Stokes parameters I, Q, U, and V. The degree of linear polarization is given by $\sqrt{Q^2 + U^2}/I$, with the position angle of the electric vector $PA = 0.5 \arctan(U/Q)$. In absence of Faraday rotation, which is a reasonable assumption for Jupiter (e.g., de Pater [1980]), the projection of the projected magnetic field can be found by rotating PA over 90°. Note, however, that the emission is integrated along the entire line of sight, weighted most heavily by the regions which emit most radiation. The degree of circular polarization, V/I, is a measure of the strength of the component of the magnetic field directed along the line of sight. In general, one expects zero circular polarization for a dipole field if the observer is in the magnetic equatorial plane, and maxima (with opposite sign) when the magnetic poles are facing the observer.

2.2. Jupiter's synchrotron radiation

After the "discovery" of Jupiter's synchrotron radiation (see section 1.3), this component of the planet's microwave emission has been studied in detail. The variation of the total non-thermal intensity

polarization characteristics during one Jovian rotation (so-called beaming curves) is indicated in fig. 14 for the total intensity S, the position angle PA of the electric vector, the linearly and circularly polarized polarization P_L and P_C, and the magnetic latitude of the earth, ϕ_m. The orientation of Jupiter's magnetosphere is indicated at the top. The maxima and minima in S and P_L occur approximately at $\phi_m = 0$ and $|\phi_m| = \max$ respectively, while the circularly polarized flux density is zero where S and P_L show maxima, and P_C shows a positive or negative maximum where S and P_L show minima. These curves indicate that Jupiter's magnetic field is approximately dipolar in shape, offset from the center of the planet by $\sim 0.1 R_J$ towards a longitude of 140°, and inclined about 10° from the rotation axis (see, e.g., review by de Pater and Klein [1989]). Most electrons are confined to the equatorial plane.

The magnetic north pole is in the northern hemisphere, tipped towards a longitude of 200°. The 40 MHz cutoff at decametric wavelengths implied a strength of about 10 G at the surface. When the spacecraft Pioneer 10 and in particular Pioneer 11 flew by Jupiter, all findings reported above were

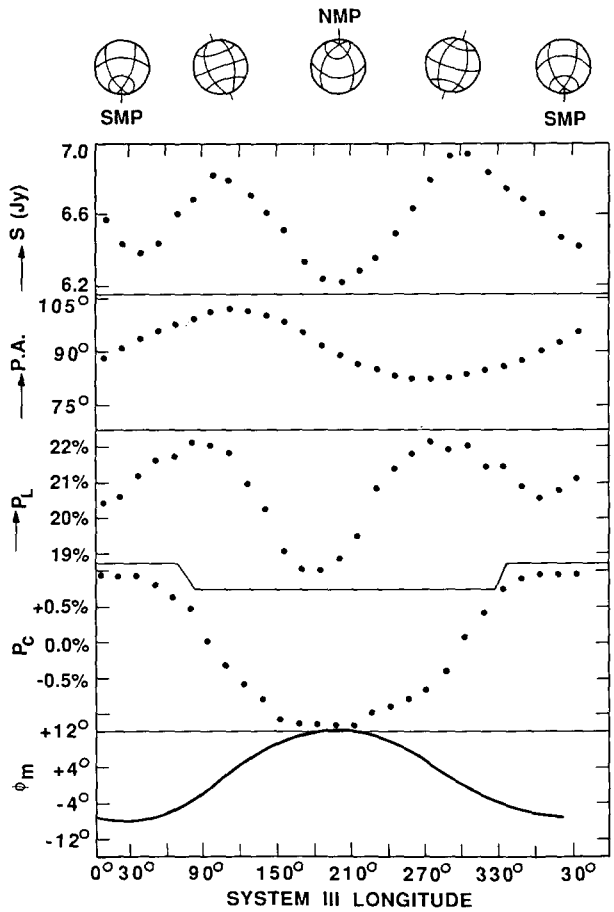

Fig. 14. An example of the modulation of Jupiter's synchrotron radiation due to Jupiter's rotation (from de Pater and Klein [1989]; after de Pater [1980]). The orientation of the planet is indicated at the top; the different panels show subsequently the total flux density S, the position angle PA of the electric vector, the degree of linear and circular polarization P_L and P_C, and the magnetic latitude of the earth ϕ_m. This latitude can be calculated with $\phi_m = D_E + \beta \cos(\lambda - \lambda_0)$, with D_E the declination of the earth, β the angle between Jupiter's magnetic and rotational axes, λ the longitude, and λ_0 the longitude of the magnetic north pole.

confirmed. However, none of the spacecraft to date passed close enough to Jupiter for detailed observations of the radiation belts. Only Pioneer 11 came to $1.6R_J$, but along a fast north–south track. Due to this relatively close approach the quadrupole and octupole terms of the magnetic field could be measured with a reasonable accuracy. This, together with the information on particles at larger distances from the planet can be used as boundary conditions to model radio data of Jupiter's synchrotron radiation (e.g., de Pater [1981a, b]).

The first radio image of Jupiter was constructed by Berge [1966] from model fits to visibility data obtained with the Owens Valley interferometer at 10.4 cm. His result is shown in fig. 15. It shows a peak in emission at approximately $1.6R_J$ at each side of the planet (all distance scales are counted from the planet's center, and expressed in planetary radii). When telescope arrays were built (e.g., the one-mile E–W telescopes in Cambridge and Westerbork, the 5 km E–W array in Cambridge, and the Y-shaped VLA), the visibility data could be Fourier-transformed directly to yield an image of the planet. The first direct image [Branson 1968] showed a clear asymmetry between the radiation peaks – one of the peaks appeared stronger, while the ratio between the peaks changed with the planet's rotation. This was interpreted to be due to a "hot spot" in Jupiter's radiation belts, near the longitude of the magnetic north pole. Data taken six years later [de Pater and Dames 1979] showed the "hot spot" at a longitude of 255°; the 60° migration of this region is still not understood [de Pater and Klein 1989]. The first "snapshot" images, images which showed a rotational smearing of only 15° as opposed to the 120° in Branson's [1968] maps, were obtained with the Westerbork telescope [de Pater 1980], an East–West array of 12 (presently 14) dishes. Excellent images in all four Stokes parameters were obtained. The asymmetry between the radiation peaks was clearly visible, and changed from one rotational aspect to the next. A sample of the images is shown in fig. 16. Images in the circularly polarized flux component show to first approximation the changing polarity and flux density as expected for a rotating dipole field; the radiation is severely modified, however, by the non-dipole character of the field, causing large E–W asymmetries in these images (see fig. 16).

De Pater [1981a, b] developed an elaborate model to simulate the radio images, using the Pioneer results to constrain the model. She used the multipole magnetic field configuration as determined by the Pioneer spacecraft, and calculated the electron distribution using adiabatic theory and a diffusion model consistent with the Pioneer results. The O4 octupole magnetic field model as derived from the Pioneer data by Acuna and Ness [1976] appeared to fit the radio data best. She further needed an electron spectrum which was flatter than that measured by the spacecraft; this was later confirmed with calculations by de Pater and Goertz [1990], who attributed the increasing flatness of the spectrum with

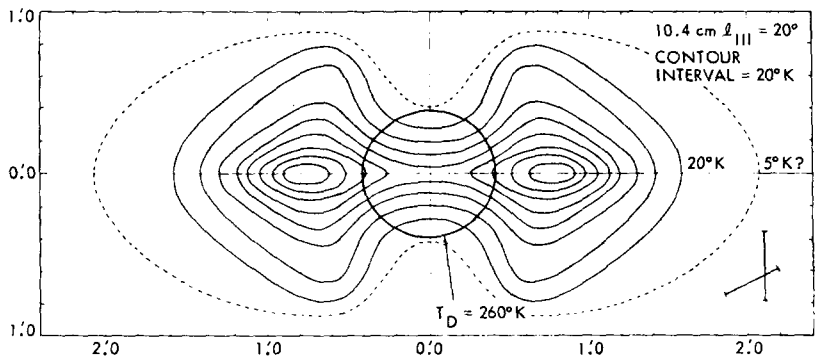

Fig. 15. A map of the brightness distribution of Jupiter's synchrotron radiation at a wavelength of 10.4 cm (from Berge [1966]). The contour interval is 20 K, and the central meridian longitude is roughly 20°. A disk component of 260 K was subtracted.

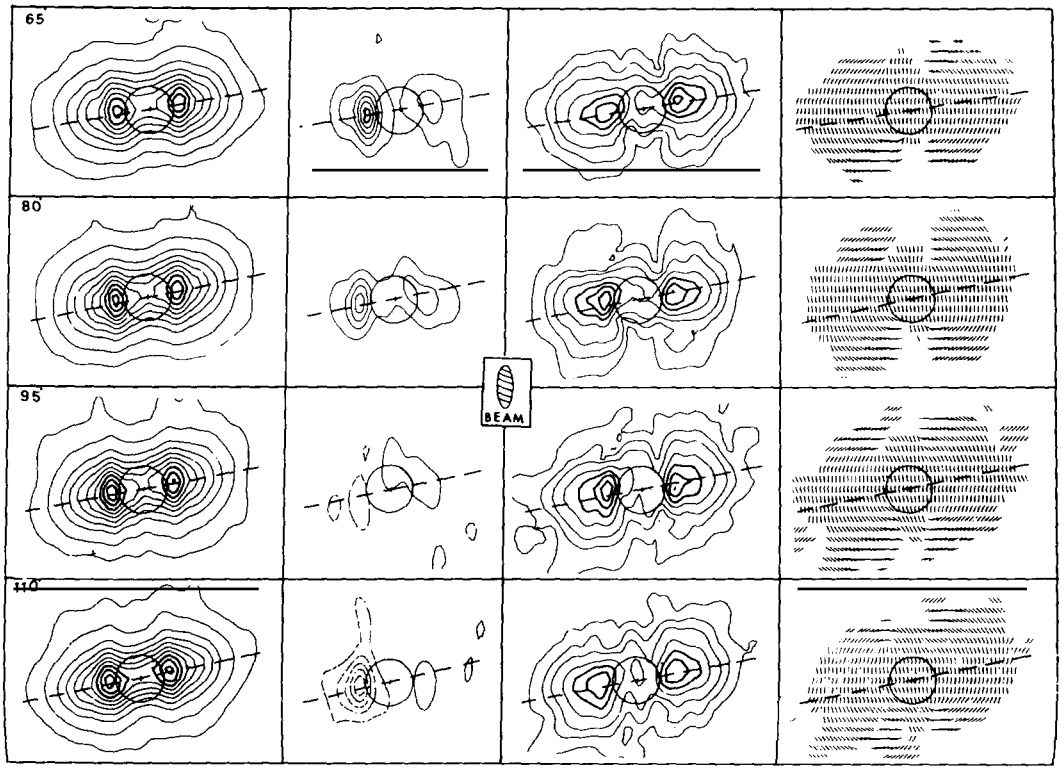

Fig. 16. Images of Jupiter's flux density as obtained with the Westerbork Radio Telescope (from de Pater [1980]). Indicated are from left to right maps of the total intensity, I, the circularly and linearly polarized flux densities, V and P, and a vector diagram of the magnetic field of the planet. Dashed contours indicate left handed, fully drawn contours right handed circular polarization. The contours belonging to the three highest values in all three maps are drawn with heavy lines. The central meridian longitude is indicated in the top left corner. Contour values are: for I, 9.5 K, 65–1065 K in steps of 125 K; for V, 1.9–21.5 K in steps of 2.8 K; for P, 9.5, 32, 65–325 K in steps of 65 K.

decreasing distance to the planet to scattering by the dust particles in the planet's rings and general environment. Absorption effects by the satellites Thebe and Amalthea, as well as the ring cause the electron distribution to be confined to the equatorial plane. The "hot spot" could partly be explained by the multipole character of the field together with a dusk–dawn electric field over the magnetosphere. An excess of electrons, however, is still needed near longitudes of 240°–360°.

In later years, high resolution images of Jupiter's synchrotron radiation were obtained by Roberts et al. [1984] and de Pater and Jaffe [1984] using the VLA at 20 cm. One of the images is displayed in fig. 17. It reveals more details of the emission, and visually confirms the confinement of the radiation to the magnetic equatorial plane out to a distance of approximately three Jovian radii, the orbital distance of the satellite Thebe. The most intriguing new features are the secondary emission peaks just north and south of the main peaks. They must be produced by electrons at their mirror points, implying a rather large number of particles between $2.5R_J$ and $3R_J$ with small pitch angles [de Pater 1983], not seen by any spacecraft nor predicted from de Pater's [1981b] model calculations.

2.2.1. Time variability

For a detailed review on the time variability in Jupiter's synchrotron radiation the reader is referred to the paper by de Pater and Klein [1989]. Their paper is summarized below.

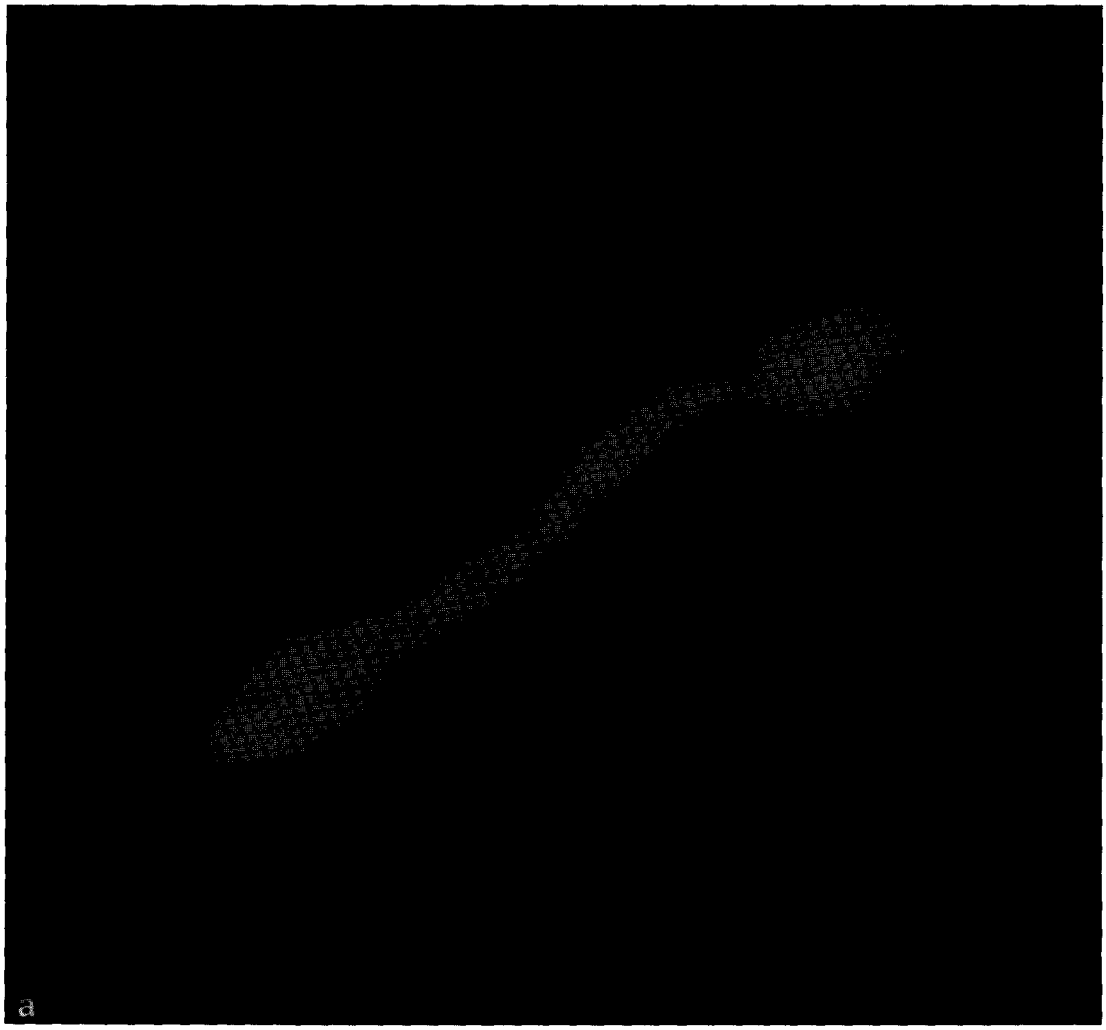

Fig. 17. (a) a radio photo and (b) a contour map of Jupiter at a wavelength of 20 cm. The radio photo is at a central meridian longitude of 117°, the contour map at 200°. Contour values are: 119, 178, 237, 297, 356, 416, 475, 594, 712, 831, 950, and 1070 K.

Only a few years after the first detection of Jupiter's synchrotron radiation in 1958 [Sloanaker 1959], Roberts and Huguenin [1963] reported data which suggested that the intensity of Jupiter's radiation was correlated with solar activity. The reality of the fluctuations was much debated due to possible confusion with background radio sources. However, subsequent observations by Gerard [1970], Klein et al. [1972], Gerard [1976] and Klein [1976] showed that long term variations occurred in the planet's flux density, but that they were not correlated with the solar 10.7 cm flux. Gerard [1970, 1976] reported the existence of irregular short term variations. A typical timescale for these fluctuations was about one week.

Since 1971 the planet has been monitored with the 26-meter Goldstone antenna in California [Klein et al. 1989], at a wavelength of 13.1 cm. Figure 18 shows the observations as a function of time [Klein et al. 1989]. The database is extended with 11–13 cm observations taken prior to 1969 from the Parks

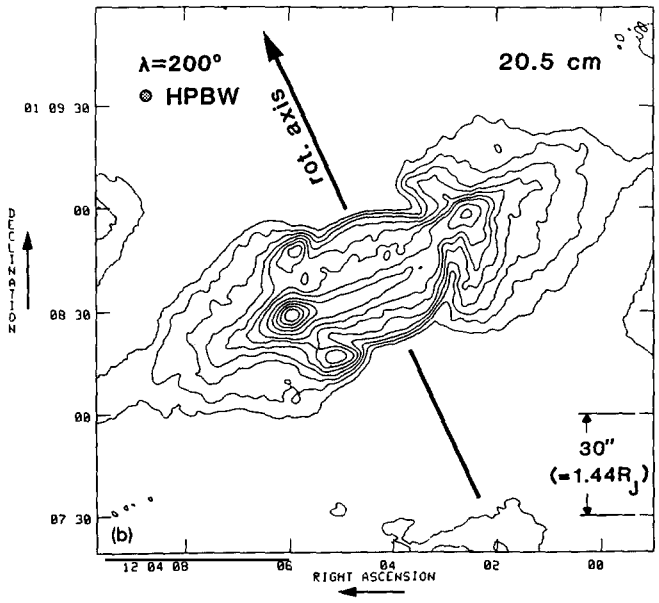

Fig. 17b.

(Australia) and Nancay (France) telescopes (see Klein [1976]). A clear long term variation in the flux density can be distinguished, with several irregular shorter term variations.

In addition to the time variability detected in the total intensity, a few other characteristics may change as well. In the period between 1967 and 1973 the following changes were apparent [de Pater and Klein 1989]. The 11–13 cm intensity decreased by ~25%, while the flux density at 20 cm dropped by ~35%, which hints at a hardening of the spectrum. Further, the standoff distance of the radiation peaks decreased, while the "hot spot" migrated 60° in longitude. The migration of the "hot spot" could imply a change in the higher order moments of the magnetic field configuration. If true, the diffusion parameters and wave–particle interactions would all be influenced. This, for example, can cause an

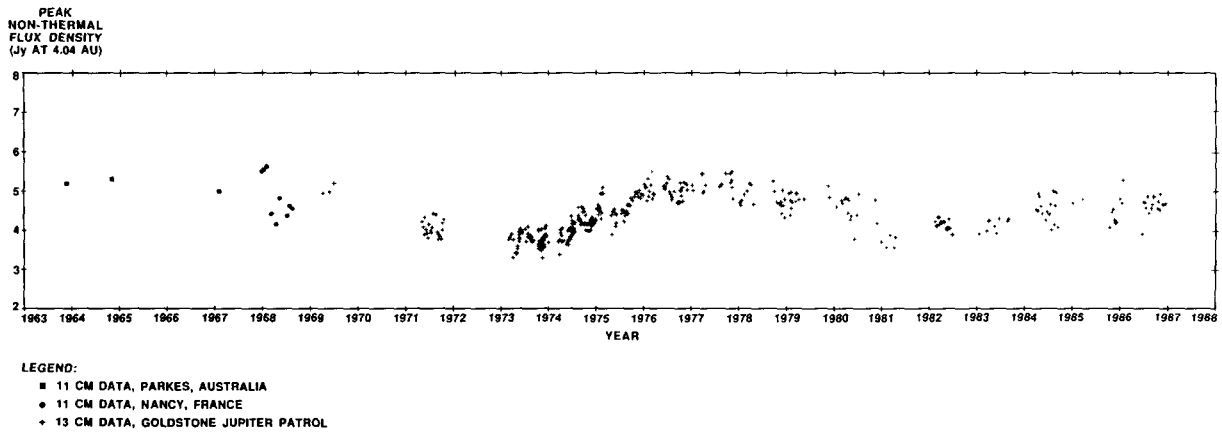

Fig. 18. The peak non-thermal flux density from Jupiter at 11–13 cm wavelength as a function of time (from Klein et al. [1989]).

increased loss of particles into the atmospheric loss cone, which would result in a corresponding decrease in the synchrotron emission. Of course, the electron spectrum may have changed as well, since wave–particle interactions are generally energy dependent. It may be difficult to sort out the various explanations until new results can be obtained from earth based observations and/or from the Galileo spacecraft.

Between 1972 and 1977 the radio emission from Jupiter increased steadily and the radiation peaks moved outwards. The shape of the beaming curves in the various synchrotron radiation characteristics remained constant during these years (except for changes which can be explained by the changing viewing geometry), which suggests that the magnetic field configuration did not change significantly. Hence the slow increase in Jupiter's flux density and in the standoff distance of the radiation peaks is probably caused by fluctuations in the particle density and/or the diffusion parameters, although fluctuations in the overall magnetic field intensity cannot be excluded.

Recently, Bolton et al. [1989] finished a correlation study of the time variability in Jupiter's total flux density with fluctuations in various solar wind parameters. They noticed a possible positive correlation with the solar wind density (or actually, the thermal wind ram pressure and thermal pressure parameters involving the density). Their analysis suggests a typical delay time between fluctuations in the solar wind and changes in the Jovian synchrotron radiation of about two years. This hints at the solar wind influencing the supply and/or loss of electrons to Jupiter's inner magnetosphere.

2.3. Conclusions

Detailed images of Jupiter's non-thermal radio emission have considerably improved our knowledge regarding Jupiter's field and electron distribution. The magnetic field configuration is best represented by the O4 magnetic field model [Acuna and Ness 1976], which was based upon the Pioneer results. The satellites Thebe and Amalthea cause the electrons to be confined to the magnetic equatorial plane. Energy degradation of the electrons by dust in Jupiter's ring harden the electron spectrum considerably. From a comparison between the time variability in Jupiter's synchrotron radiation and that seen in solar wind parameters, it appears that the solar wind does influence the supply and/or loss of electrons to Jupiter's inner magnetosphere.

The following outstanding issues still need to be fully resolved, however.

(1) The existence of the "hot region" which may be partly caused by higher order moments in Jupiter's field.

(2) The existence of secondary emission features north and south of the main radiation peaks, which are presumably caused by the presence of small pitch angle electrons in Jupiter's radiation belts, at equatorial distances between 2 and 3 Jovian radii.

(3) Time variability; although much progress has been made by Bolton et al. [1989] on the long term time variations in Jupiter's synchrotron radiation, the short term variations have not even been confirmed. If real, they need to be interpreted. Other synchrotron radiation parameters which have changed over the past decades are the standoff distance of the radiation peaks, the longitude of the "hot spot", the radio spectrum, and possibly the modulation of the position angle of the electric vector as a function of Jovian longitude. None of these phenomena are yet understood.

(4) A solution to all or some of the above points may help to find the source and mode of transport of the high energy electrons in Jupiter's inner radiation belts.

3. Terrestrial planets

3.1. Introduction

Microwave observations of Mercury, Venus, and Mars probe the atmosphere as well as the (sub)surface layers of the planets. Both Venus and Mars have atmospheres which consist primarily of CO_2 gas, which is the primary source of atmospheric microwave opacity. The photolysis product of CO_2, CO, has strong rotational transitions at millimeter wavelengths, which can be utilized to determine the atmospheric temperature profile and the CO abundance on Venus and Mars in the altitude regions probed.

The temperature structure of the (sub)-surface layers of airless bodies depends upon a balance between solar insulation, heat transport within the crust, and reradiation outward. The conductive heat transport into the subsurface depends upon the thermal conductivity and the heat capacity of the material; reradiation from the surface depends upon the emissivity of the material. The emissivity is described by the dielectric constant, ε, and loss tangent of the material, $\tan \Delta$, which are determined by the bulk density or composition of the material and its state of compaction (e.g., Campbell and Ulrichs [1969]). A typical radio skin depth is about ten wavelengths. Hence, by obtaining a spectrum of the objects, properties regarding its (sub)surface layers can be derived. However, since most constants entering the equations for heat conduction and radiative transfer outward vary with wavelength as well as composition of the material, interpretation of such spectra remains very difficult. In addition, scattering in the subsurface layers may be important as well, but is generally neglected.

If an atmosphere overlies the crust of the planet, the crust can be dramatically heated by the greenhouse effect in the atmosphere. Venus' surface, for example, is warmer by a factor of about 3 as compared to the temperature expected from solar insulation alone. Thus models including both the atmosphere and crust layers need to be developed (e.g., Muhleman et al. [1979]).

3.2. Mars

3.2.1. Surface

Due to the variation in heliocentric distance, r_m, Mars' surface brightness temperature will vary as $r_M^{-0.5}$. The temperature of the crust may be slightly increased above that expected from solar illumination by the atmospheric greenhouse effect. In addition, although atmospheric dust storms are transparent at radio wavelengths, these storms may have a direct influence on the Martian flux; the dust particles contribute to the opacity at wavelengths shorter than about 40 μm, and therefore affect the temperature gradient in the atmosphere and reduce the amount of solar radiation to the surface, thus causing a decrease in the surface brightness temperature. The latter effects have not yet been taken into account in modeling efforts of Mars' surface.

Sunlight will heat Mars' surface during the day; the heat will be transported downwards mainly by conduction. The amplitude and phase of the diurnal temperature variations, and the temperature gradient with depth in the crust are largely determined by the thermal inertia, $\gamma = (K\rho C)^{1/2}$, and the thermal skin depth of the material, $L_t = (2K/\Omega\rho C)^{1/2}$. In these expressions K is the thermal conductivity, ρ the density of the material, C the heat capacity, and Ω the angular velocity. Temperature variations are largest at the surface, where the temperature is determined directly by the solar radiation. Obviously, the insulation is largest at noon, and absent at night. Since the heat is transported downwards by conduction, it takes time for the subsurface layers to heat up. Thus we see a phase lag in

the diurnal temperature variation, and the amplitude of the variation will be diminished. When the thermal inertia, or more precisely the thermal conductivity, is low, the amplitude of the temperature wave is large and does not penetrate deeply into the crust. If the inertia, or thermal conductivity, is high, temperature variations are smaller, but penetrate to greater depths in the subsurface layers.

Disk-averaged brightness temperatures of Mars at infrared as well as radio wavelengths show a variation with central meridian, or sub-earth, longitude (CML) [Andrew et al. 1977; Epstein et al. 1983]; data at 20 μm, 3.5 mm, and 2.8 cm during Mars' 1978 opposition are shown in fig. 19 [from Epstein et al. 1983]. Note that all observations are of Mars' day side; we cannot observe the night side from the ground. Since the disk-average surface temperature of the planet will be higher than the temperature of the subsurface layers, the 20 μm brightness temperature is higher than the radio brightness temperature (note: differences in emissivity between the wavelengths can cause such effects as well). The temperature variations at infrared wavelengths are out of phase with those at radio wavelengths, which can be understood in terms of the thermal inertia or conductivity discussed above. Thus, regions with a low inertia will have a high brightness temperature at infrared wavelengths, and a low temperature at radio wavelengths. Epstein et al. [1983] show that the reversal between the curves should occur at a wavelength between 0.2 and 3 mm; thus the longitudinal variation should be absent at that wavelength. One can see in fig. 19 that the rotation curve amplitude at 3.5 mm is larger than that seen at 2.8 cm and 20 μm; Epstein et al. attribute this to surface scattering from rocks or roughness on a scale less than 1.5 cm.

Rudy [1987] and Rudy et al. [1987] imaged Mars at 2 and 6 cm, using the VLA in the most extended, or A, configuration. They obtained data in both the total intensity and polarized flux density. The latter is useful to determine the dielectric constant of the surface. Two seasons were observed: late spring in the northern hemisphere (at a planetocentric orbital longitude $L_s \sim 60°$; beginning of spring is at $L_s = 0°$) and early summer in the southern hemisphere ($L_s \sim 305°$). One of the images is shown in fig. 20 (Rudy, private communication). From these data Rudy determined the variation in brightness temperature with latitude on the planet; since the data were smeared in longitude, no longitudinal

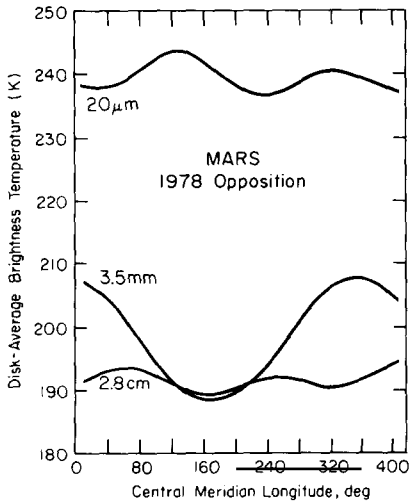

Fig. 19. Best fits (from Epstein et al. [1983]) to the disk-averaged Martian brightness temperature at 20 μm, 3.5 mm, and 2.8 cm, as a function of central meridian longitude. The data were taken during the 1978 Mars opposition period.

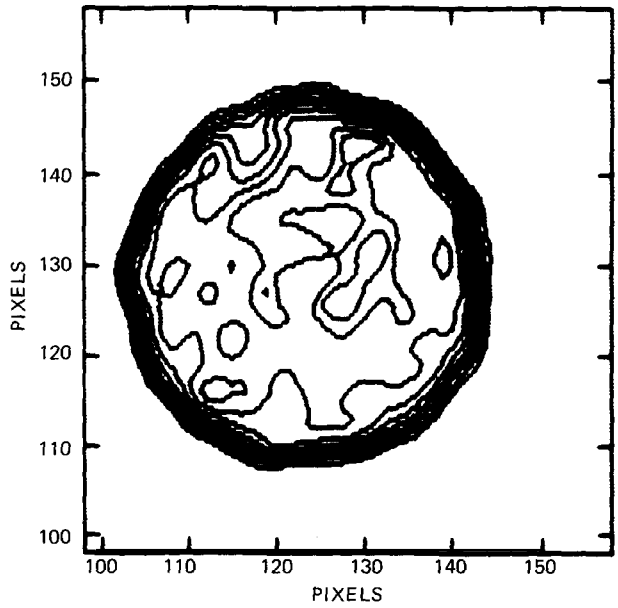

Fig. 20. A contour map of Mars at 6 cm wavelength (from Rudy, personal communication). The HPBW is 0.45", the diameter of Mars 4.44". Contour values are approximately: 45, 67, 90, 112, 135, 157, 180, 202, and 213 K.

information could be obtained. On both the northern and southern hemisphere there is a region near the polar caps which has a lower brightness temperature at 2 and 6 cm wavelength. Table 3 summarizes disk-averaged brightness temperatures, dielectric constants, subsurface densities, and the brightness temperature of the cold poles for both sets of observations.

Rudy et al. [1987] point out that the cold polar regions are likely due to the presence of CO_2 frost on the surface. The thickness of the frost, the distribution with space as well as depth into the crust, all modify the microwave brightness temperatures. Note, further, that the surface of Mars never gets much colder than the sublimation temperature of CO_2, while the temperature of layers underneath the CO_2 frost can be higher than the sublimation temperature.

Table 3
Properties of Mars' surface as derived by Rudy [1987] from VLA observations at 2 and 6 cm, in two different seasons: during the first observations, the northern, and the second the southern hemispheres were visible. The whole disk brightness temperatures are normalized to a solar distance of 1.524 AU

wavelength	2 cm		6 cm	
hemisphere	North	South	North	South
Whole disk brightness temperature	189 ± 7	198 ± 7	187 ± 5	192 ± 5
Whole disk dielectric constant	2.34 ± 0.05	2.02 ± 0.03	2.70 ± 0.09	2.47 ± 0.06
Whole disk subsurface density	1.24 ± 0.16	1.02 ± 0.16	1.45 ± 0.18	1.31 ± 0.16
polar cold region	126 ± 7	183 ± 7	150 ± 5	148 ± 5

Mars is often used as a calibrator source, and with that in mind, Rudy [1987] developed a program to calculate the microwave emission from Mars' subsurface layers, taking into account the solar insulation effect, and the heat lost to the formation or gained from the sublimation of CO_2 frost. The thermal inertia and albedo were varied across the disk in a manner consistent with the Viking results. His thesis contains the results for the disk-averaged brightness temperature as a function of Martian season, longitude, and sub-earth longitude and latitude, for calculations with dielectric constants between 1.4 and 3.8, and radio absorption lengths between 5 and 300 cm. In the future, when variations over the disk in the dielectric constant and absorption length can be constrained, the models can be updated to include those effects. Unfortunately, Rudy's VLA images are not yet sensitive enough to define clear latitudinal variations in these parameters.

3.2.2. Atmosphere

Mars' atmosphere can be probed at millimeter wavelengths, in the $J = 1–0$ and $J = 2–1$ rotational transitions of CO. CO is produced by photodissociation of CO_2, the primary constituent of Mars' atmosphere. Whether the line is seen in emission, absorption, or a combination thereof, depends mainly on the temperature–pressure profile in the atmosphere, and how this compares to the brightness temperature of the surface. The Viking temperature profiles [Seiff and Kirk 1977] show a roughly constant temperature of 140 K down to an altitude of about 60 km, below which it increases to ~210–220 K at the surface. The 115 and 230 GHz ^{12}CO lines are optically thick; thus the core of the line is formed high up in the atmosphere where it is cold, and hence is seen in absorption against the continuum background from the planet's surface. The wings of the line are formed in the lower atmosphere, just above the surface. As a consequence of the surface emissivity the brightness temperature of the surface is somewhat less than the kinetic temperature in the atmosphere just above it. The wings of the line are therefore seen in emission against the continuum background. An example of CO spectra in the $J = 1–0$ and 2–1 transitions is shown in fig. 21 (from Schloerb [1985]), these spectra were obtained during Mars opposition in 1984.

Photolysis of CO_2 proceeds at a rate of $\sim 10^{12}$ cm^{-2} s^{-1} [Hunten 1974], while recombination of CO and O ($CO + O + M \rightarrow CO_2 + M$) is very slow. Therefore the photo–chemical lifetime of CO is approximately three years. Yet, the mixing ratio of CO is only $\sim 10^{-3}$. This suggests a catalytic recombination. Hunten [1974] suggested catalysis by odd hydrogen (H, OH, HO_2), aided by very rapid downward mixing and photolysis of H_2O_2. Due to sublimation and freezing the abundance of odd hydrogen is rather unstable, which can lead to changes in the CO abundance by a factor of about 2 on a timescale of about one year. Based upon the Phobos/UV, visible and infrared data Atreya and Blamont [1990] proposed that heterogeneous chemistry between CO and O involving aerosols may play a major role in the recombination process. Due to large spatial as well as time variations in the abundance of such particles, the CO abundance may locally change on timescales as short as ten days.

Time variability in CO on timescales between months and years has been reported more than once [Good and Schloerb 1981; Clancy et al. 1983; Lellouch et al. 1989]. Since the determination of the CO abundance and choice of temperature–pressure profile both influence the line profiles, a unique solution of the CO abundance can only be found if measurements of both the optically thick ^{12}CO and optically thin ^{13}CO lines are made. Clancy, Muhleman and Berge (personal communication) analyzed CO microwave spectra and suggest a constant CO mixing ratio (averaged over the disk!) with time between 1967 and 1988, but a distinct change in the temperature–pressure profile. Images of Mars in the CO lines might shed some light on possible spatial variations in the CO abundance with latitude and local time, which will likely help to get a better understanding of the production and destruction of CO

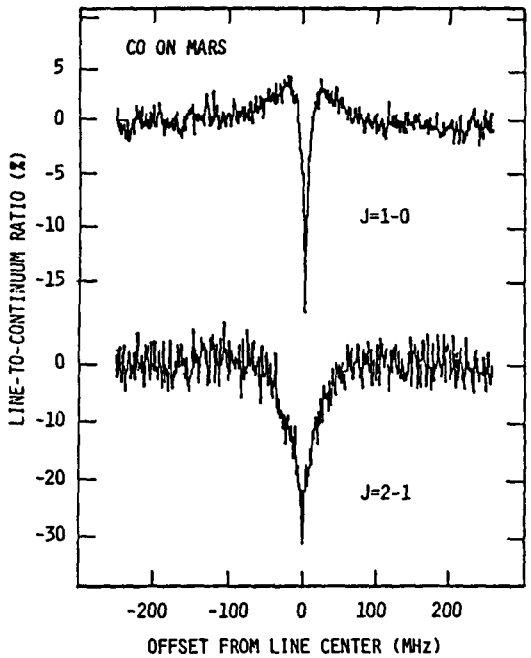

Fig. 21. Spectra of Mars in the CO $J = 1-0$ and $J = 2-1$ transitions, during the 1984 opposition (from Schloerb [1985]).

in Mars' atmosphere. Such data have recently been obtained at 3 mm with the Hat Creek Radio Interferometer by Mitchell during Mars' opposition in 1988. In addition to the science regarding the atmosphere, the 3 mm continuum images of Mars' surface will contribute to our knowledge of the surface characteristics of the planet.

3.3. Venus

3.3.1. Spectrum

Microwave observations of Venus probe the atmosphere and, at wavelengths longwards of about 4 cm, the surface. A spectrum of the disk-averaged brightness temperature is shown in fig. 22 [from Muhleman et al. 1979]. Between a few millimeters and 7 cm the brightness temperature increases from ~300 K to ~650 K. At the longer wavelengths one probes deeper levels in the atmosphere, which, due to the adiabatic temperature structure in Venus' atmosphere, results in the steep temperature increase in the spectrum. There are no diurnal temperature variations, due to the large heat capacity of the atmosphere. At wavelengths longwards of 7 cm the subsurface layers of the planet are probed. In order to interpret Venus' radio spectrum, a model needs to be developed which includes both the atmospheric and surface emission/absorption characteristics. Such a model was developed by Muhleman et al. [1979]; their result is superimposed on the data in fig. 22.

3.3.2. Surface

Chapman [1986] and Pettengill et al. [1988] imaged Venus at 6 and 20 cm wavelength with the VLA. The left-hand side of fig. 23 shows an image at 20 cm, taken on November 12, 1983. The Aphrodite

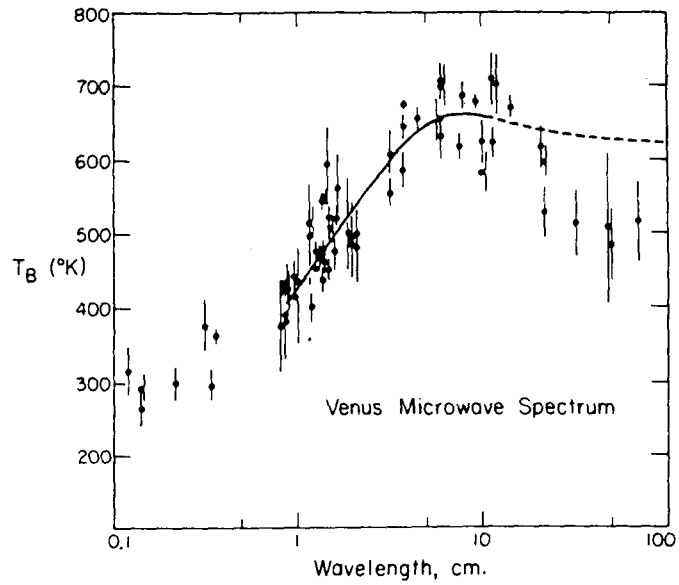

Fig. 22. Venus microwave spectrum with the model of Muhleman et al. superimposed (from Muhleman et al. [1979]).

region is near the center of the planet, and the two cool regions coincide with the locations of Thetis and Ovda. The brightness temperatures of the latter regions are 515 K and 450 K respectively, compared to the disk-averaged temperature of 636 ± 28 K. The high brightness temperature to the north of the Aphrodite region has a peak value of 772 K. From the radio brightness temperatures one can obtain the emissivity of the material, if the physical temperature of the observed region is known. With a surface temperature of 735 K and vertical adiabatic lapse rate of 8 K/km (e.g., Seiff [1983]), the

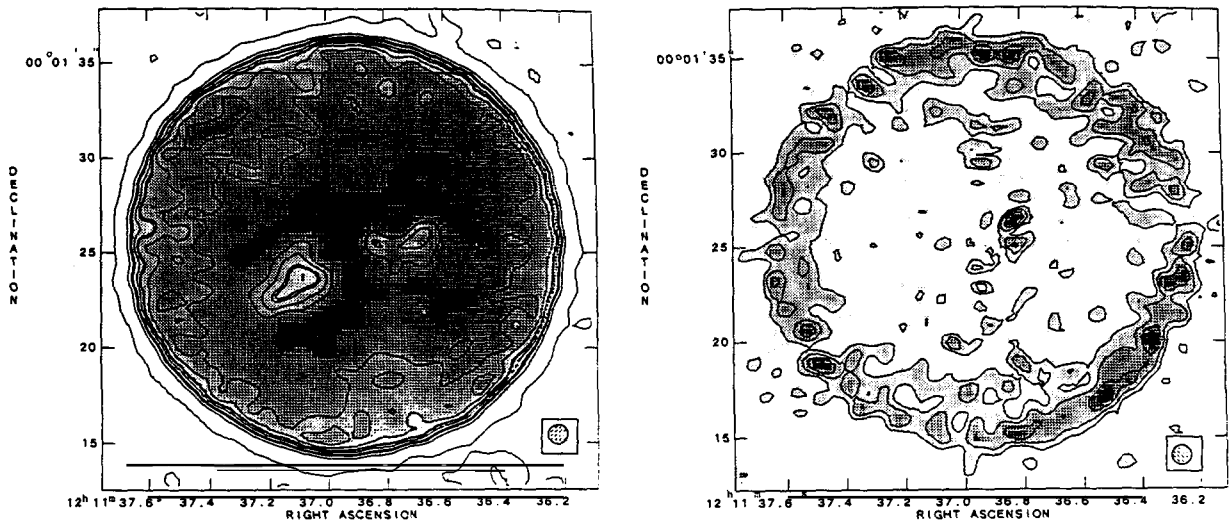

Fig. 23. Radio images of Venus (from Chapman [1986]). Left: the total intensity; contour levels are: 90, 315, 371, 382, 405, 450, 483, 494, 539, 584 K. Right: linearly polarized flux density; contour values are: 0.1, 0.15, 0.2, 0.25 mJy/beam.

temperature of the mountains can be calculated if the altitude of the area is known (from, e.g., radar observations). The Thetis and Ovda regions appear to have emissivities of 0.71 and 0.62 respectively, while the disk-averaged value is 0.86. The latter value implies a dielectric constant for the material of 5, in close agreement with the radar results. The low emissivities of the Thetis and Ovda regions imply dielectric constants as high as 20–30.

Information on the dielectric constant can also be obtained from images of the polarized intensity [Chapman 1986]. The right-hand side of fig. 23 shows the intensity of the linear polarization for the image shown on the left-hand side. Note that the polarized intensity increases as one approaches the limb. At transmission angles less than 30°–40°, the signal is buried in the noise. At larger angles the signal-to-noise ratio improves, and the dielectric constant can be determined. The data suggest ε to decrease with increasing angle of transmission, from a value close to 4 at transmission angles near 30°, down to 2.5 near the limb. These values are lower than those obtained from the radio emissivities and the radar reflectivity data. This fact, as well as the apparent decrease in the dielectric constant when approaching the limb, may be caused by surface roughness, which will reduce the degree of polarization. An alternative explanation would be the existence of a vertical gradient in the density of the surface material.

Venus' surface properties can only be determined from the VLA images when combined with the radar results. The radar scattering and reflectivity characteristics contain additional information on the (sub) surface properties of the planet. Pettengill et al. [1988] analyzed results from the Pioneer Venus radar altimetry experiment in combination with the VLA measurements. The radar data show that the reflection coefficient varies over the disk from 0.14 ± 0.03 in the lowlands to roughly 0.40 in the highlands. Regions with a high reflectivity show low brightness temperatures (on VLA images as well as the temperature measured by the Pioneer Venus radiometer), thus a low emissivity. Table 4 gives details on the parameters for the regions which can be distinguished on the different VLA images. The emissivities of the regions were obtained from the brightness temperatures measured in the VLA images, combined with those obtained from the Pioneer Venus radiometer.

The results of the planet's emissivity (and hence dielectric constant) can be interpreted in terms of its surface composition [Chapman 1986; Pettengill et al. 1988]. Dielectric constants of about 2 imply porous surface materials; $\varepsilon \sim 5$–9 is typical for solid rocks (granite–basalt). Much higher dielectric constants can be caused by the inclusion of metallic and/or sulfide material. Hence, Venus' surface is overlain, at most, by only a few centimeters of soil or dust, and probably consists of dry solid rock. The highlands probably contain substantial amounts of minerals and sulfides close to the surface. On earth, such material is often formed in volcanic areas.

Table 4
Properties of Venus' surface (after Pettengil, Ford and Chapman [1988])

Feature	reflection coefficient	brightness temperature	estimated physical temperature	emissivity	dielectric constant
Lowlands or whole disk average	0.14 ± 0.03	636 ± 28	735	0.86 ± 0.04	5.0 ± 0.9
Maxwell Montes	0.40 ± 0.05	420 ± 25	663	0.50 ± 0.07	38.7 ± 15.0
Ovda region	0.39 ± 0.05	450 ± 35	695	0.55 ± 0.06	24.3 ± 8.8
Thetis region	0.37 ± 0.08	515 ± 35	703	0.60 ± 0.07	20.5 ± 9.0

3.3.3. Atmosphere

Muhleman et al. [1979] modeled Venus' spectrum, and concluded that the atmospheric opacity is due to CO_2 gas and some unknown absorber. Steffes [1985, 1986] suggests that the extra absorptivity in Venus' atmosphere at microwave wavelengths longwards of 1.8 cm is due to H_2SO_4 gas, and at $1.2 < \lambda < 1.8$ cm to SO_2 gas. Both the CO_2 and SO_2 absorptivities vary as λ^{-2}, but the H_2SO_4 opacity shows a pronounced peak at 2.2 cm. Steffes et al. [1990] obtained a good fit to Venus' radio spectrum using a model atmosphere with the microwave absorbers CO_2, H_2SO_4, and SO_2. They assumed an abundance of 96% for CO_2. The SO_2 abundance was taken to be zero above the cloud layer (>48–50 km), and 40 ppm below the main cloud layer down to the surface. Gaseous H_2SO_4 was assumed to be uniformly distributed at 5 ppm between 38 and 48 km; it is fully dissociated at lower levels, and above 48 km condensation starts, and the gas follows the saturated vapor curve.

Unfortunately, we do not yet have images of Venus' atmosphere at short centimeter wavelengths. Such images contain information on the spatial distribution of the absorbing gases, and would be extremely helpful for unraveling possible time variations in Venus' microwave brightness temperature [Steffes 1986].

At millimeter wavelengths, in the $J = 1$–0 and $J = 2$–1 transitions of the CO line, one probes altitudes between 70 and 120 km, the mesosphere of Venus, a region not well studied at other wavelengths. CO is produced upon photodissociation of CO_2 by solar UV radiation, in the 70–120 km altitude region. This is a transition region between the massive lower atmosphere (altitudes $\lesssim$70 km), in which the radiative time constant is much greater than a solar day, and the upper atmosphere (altitudes $\gtrsim$120 km) which has a low heat capacity. As mentioned before, the temperature structure in the lower atmosphere follows an adiabatic curve; in the upper atmosphere a strong day-to-night gradient in the temperature is expected and observed (e.g., Seiff [1983]). The difference in temperature structure between the two atmospheric regions will cause a very different wind pattern to exist as well. A strong retrograde zonal wind is observed in the visible cloud layers (~48–63 km altitude) with velocities of the order of ~100 m/s; in the upper atmosphere the day-to-night temperature gradient should drive strong day-to-night winds, which are recently observed by Goldstein et al. [1988]. Since CO is formed in the transition region, CO line spectra can be used to derive the thermal structure in the mesosphere, the wind speeds and direction, and the CO abundance as a function of altitude.

Because the continuum emission at millimeter wavelengths originates in the low warm part of the atmosphere, the CO lines are seen in absorption against the continuum background. The lines are pressure broadened by Venus' dense atmosphere. The $J = 1$–0 transition of this line was first observed by Kakar et al. [1976]. Since Venus' dayside hemisphere is observed when the planet is near superior conjunction, and its nightside when it is near inferior conjunction, disk-averaged spectra of both hemispheres were obtained. An example is shown in fig. 24, top part, (from Schloerb [1985]). On all spectra, the nightside is approximately three times deeper than the dayside line. Figure 24, bottom part, shows the peak absorption in the line center as a function of local time on the planet (lower panel), and the absorption in the line wings (upper panel; from Schloerb [1985]). Note that these data are all for disk-averaged spectra; the local time along the X-axis is for the sub-earth longitude.

The core of the line seems to vary symmetrically from the dayside to the nightside, and the wings of the line appear to have their peak absorption just after local midnight. These results were interpreted with a CO abundance which is larger on the night side of the planet than the dayside. This is just opposite to what one would expect, if CO is formed by photodissociation of CO_2. Clancy [1983] and Clancy and Muhleman [1985] suggested that the CO is probably carried from its place of formation at the dayside to nightside by strong day-to-night winds such as those expected to exist in Venus'

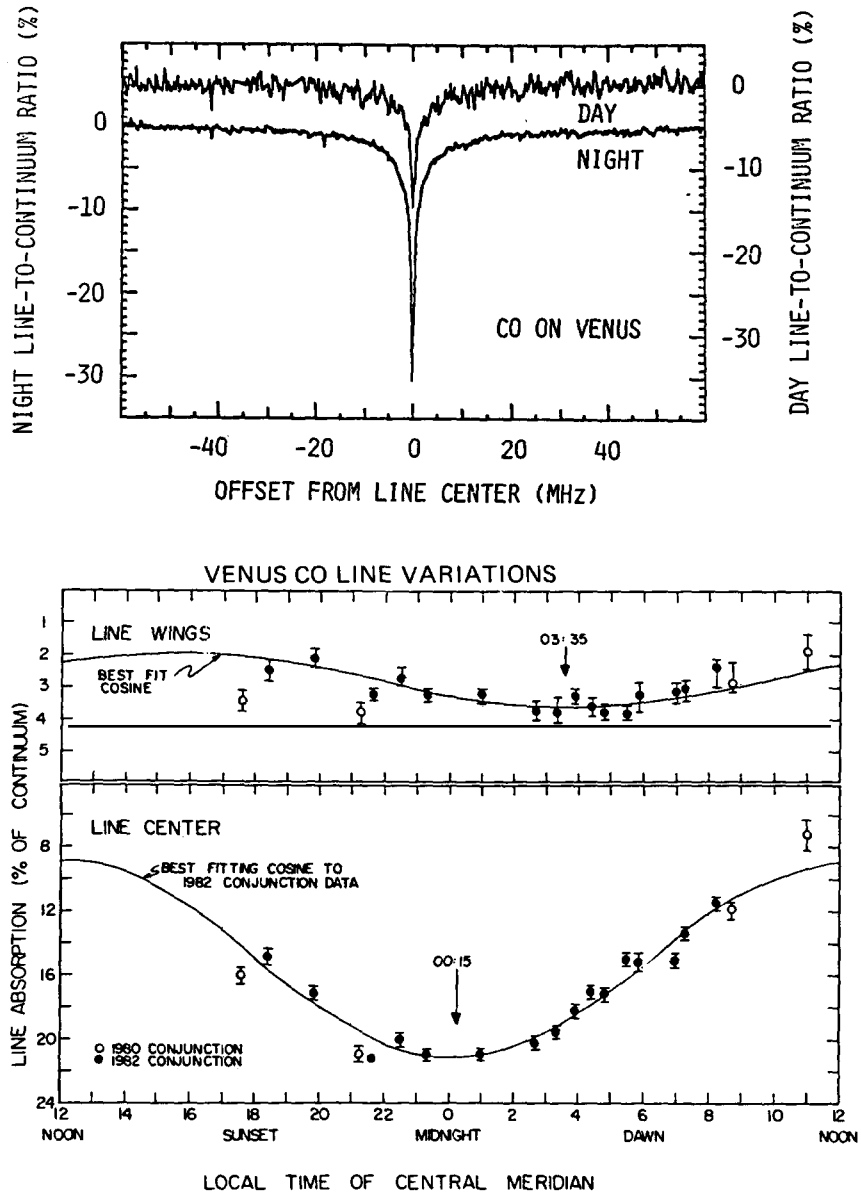

Fig. 24. Top: spectra of Venus in the $J = 1$–0 line; the upper curve is for the dayside hemisphere (when Venus is near superior conjunction), the lower curve for the nightside hemisphere (when Venus is near inferior conjunction). Bottom: variations in the line absorption at the line center (lower panel) and in the line wings (upper panel). (Results from Schloerb [1985].)

mesosphere. According to Clancy [1983], also Clancy and Muhleman [1985], a small influence of the retrograde cloud circulation on the CO abundance at the lower levels of the CO line formation (where the line wings originate, ~70–90 km) may explain the few-hour shift away from midnight in the maximum absorption of the line wings.

Recently, de Pater, Schloerb and Rudolph [1990] imaged Venus at a wavelength of 2.6 mm

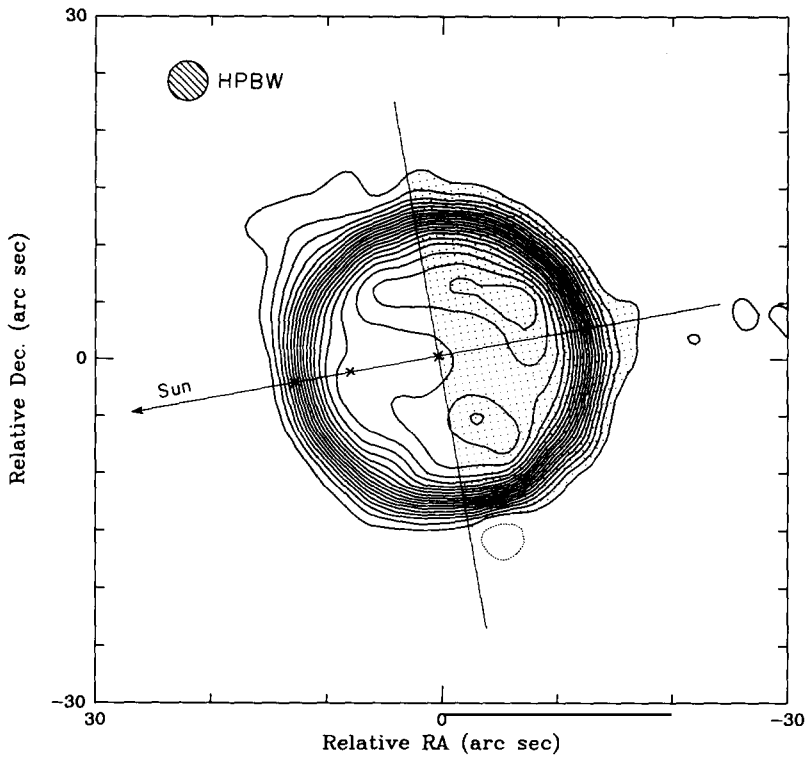

Fig. 25. Radio image of Venus at 3 mm (from de Pater, Schloerb and Rudolph in preparation). The direction to the sun and the terminator are indicated. The contour levels are in 5% intervals, with a maximum of ~365 K. The crosses along the sun–Venus line indicate the locations of the spectra displayed in fig. 26.

(112 GHz) using the Hat Creek millimeter array*) while Venus was at Western elongation (January 1987). The spatial resolution was 3.5″. Figure 25 shows the image of the 3 mm continuum emission. The nightside of the planet is warmer than the dayside, by approximately 30 K. In addition, the tropical regions at the nightside in particular in the northern hemisphere, are brighter than the equatorial band. At this wavelength we probe down in the cloud layers. Since there is no day-to-night variation in the thermal structure in this part of the atmosphere, the difference in the brightness temperature is due to a variation in opacity over the disk. The bulk of the 3 mm opacity comes from CO_2, but the abundance of the molecule is unlikely to vary from day to night. Two possible sources of opacity in addition to CO_2 are SO_2, and gaseous H_2SO_4 [Steffes 1985, 1986; Steffes et al. 1990]. In addition, although the clouds are transparent at centimeter wavelengths, we expect some absorptivity from the cloud particles at millimeter wavelengths. Unfortunately, the opacity due to sulfuric acid droplets has never been measured. The dielectric constant may be similar to that of water, in which case the optical depth is roughly 0.1–0.2 per km in the main clouddeck (Steffes, personal communication). For comparison, the optical depth at 3 mm in the main cloud deck due to gaseous H_2SO_4 (abundance 5–10 ppm) and SO_2 (abundance 100–180 ppm) is roughly 0.2–0.5 per km for each gas (Steffes, personal communication). Hence, we expect a similar amount of opacity due to gaseous and liquid H_2SO_4 as well as SO_2.

*) Operated by the University of California at Berkeley, the University of Illinois, and the University of Maryland, with support from the National Science Foundation.

The clouds on Venus form most likely from photochemically produced sulfuric acid (e.g., Esposito et al. [1983] and references therein). This process must be more effective on the day side than the night side. The day-to-night asymmetry in the 3 mm radio image of the planet may be due to small day-to-night differences in the sulfuric acid abundance. Since the gaseous H_2SO_4 probably follows the saturated vapor curve in the region of cloud formation, the larger opacity at the dayside might be due to a larger concentration of cloud particles rather than the gas at the dayside.

Together with the 3 mm continuum image of Venus, de Pater et al. [1990] also obtained images in the $J = 1-0$ CO line (115 GHz), with a frequency resolution of 1.25 MHz. In this transition altitudes well above the cloud layers are probed (90–120 km). In contrast to the continuum image, the images at the center of the line are symmetric about the subsolar point. Figure 26 shows spectra at four different

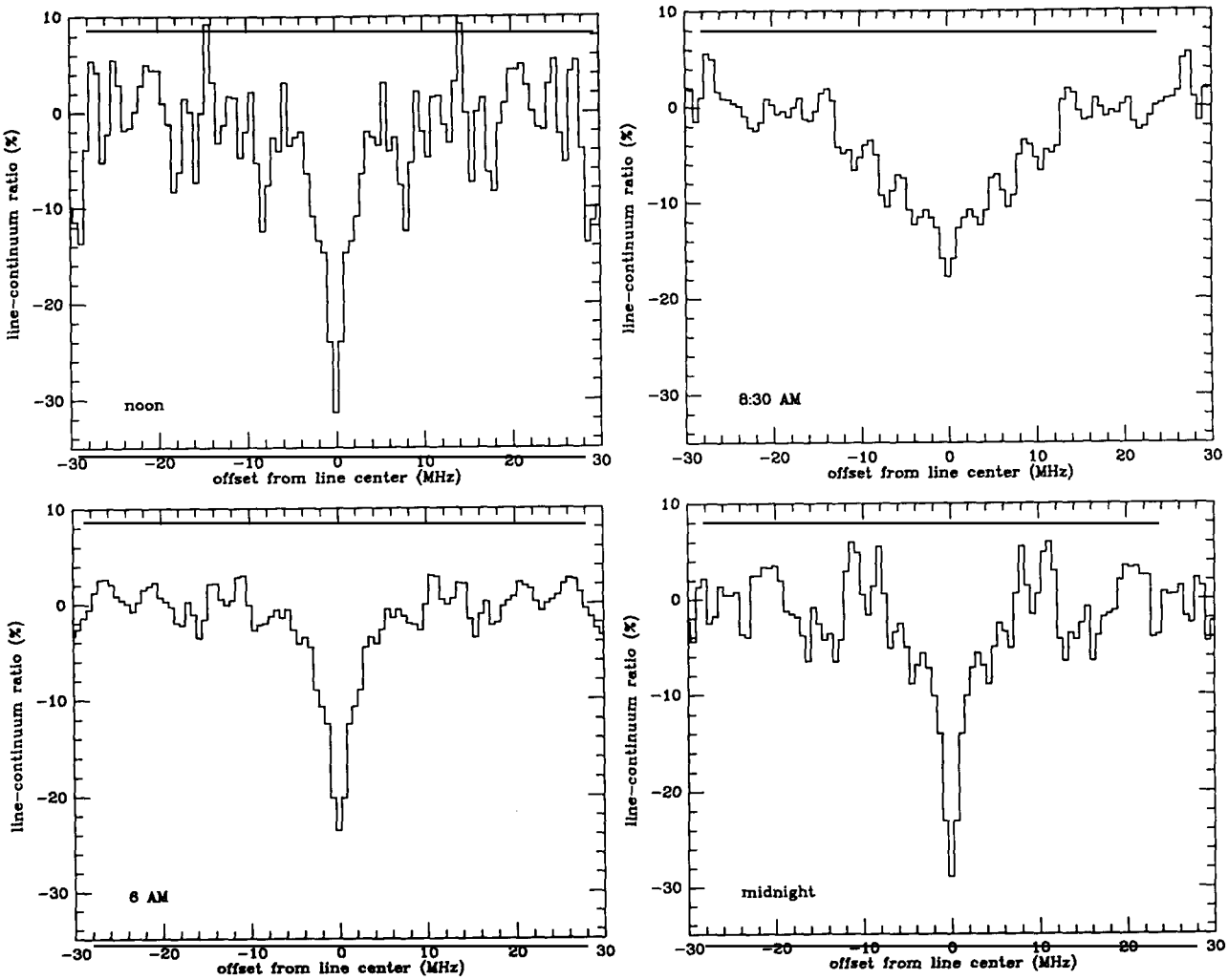

Fig. 26. Spectra at different locations on Venus' equator: noon, 9 AM, the terminator at 6 AM, and midnight. The locations are indicated by the crosses in fig. 21. The spectra are expressed in line-to-continuum ratios, and they are averaged over a Gaussian beam with FWHP 3 × 10″, with the long axis parallel to the terminator.

places along Venus' equator: upper left, at noon (the limb at the dayside); upper right, 8:30 AM (mid-morning); lower left, 6 AM (terminator); and lower right, at midnight (limb at the nightside). All the spectra are taken from the images after convolution with a Gaussian beam with FWHM of $10 \times 3.5''$, with the long axis parallel to the terminator.

The shape of the spectra varies much across the disk of the planet. On the dayside the spectra are broad and shallow, at night and at noon they are deep and narrow. Except for the line shape at noon, these results agree qualitatively with results obtained with single element radio telescopes. In addition, the above authors noticed that the CO profiles of the dayside are much broader in the northern than the southern hemisphere. The spectra were inverted to yield CO abundances at different altitudes. At low altitudes (83 km) the CO abundance is similar at all longitudes; at high altitudes (93 km), the CO abundance is smallest at the dayside, although the mixing ratio profile at noon in their images appears to be similar to that seen at night. At night, the CO abundance is similar at both altitudes, and does not change with latitude. At the dayside, the CO abundance is largest at low altitudes, and increases steadily with latitude from south to north.

3.4. Mercury

Radio observations of Mercury probe the planet's surface and subsurface layers. As on Mars, the temperature structure of these layers depends upon a balance between solar insulation, heat transport within the crust and reradiation outwards. Due to the 3/2 resonance between Mercury's rotational and orbital periods in combination with Mercury's large orbital eccentricity, the average diurnal insulation varies significantly. Regions along Mercury' equator near longitudes $\phi = 0°$ and 180° (the subsolar longitudes when the planet is at perihelion) receive roughly 2.5 times as much sunlight on the average than longitudes 90° away from it. As a result of this nonuniform heating, the diurnal temperature variation depends upon Hermographic longitude. The night time surface temperature is approximately 100 K, independent of longitude, but the peak (noon) surface temperature varies between 700 K at $\phi = 0°$ and 180° to 570 K for $\phi = 90°$ and 270° [Soter and Ulrichs 1967].

While the subsurface temperature is below that of the surface during the day, it is above the surface temperature at night. Thus, heat is transported downwards during the day, and upwards at night. Since the thermal conductivity and heat capacity depend upon the temperature of the crust, downward conduction is very effective during the day, when the surface temperature is high. At night the cold surface acts like an insulator, since conduction is very slow. In addition, due to the phase lag between solar insulation and heat transport downwards, the highest subsurface temperature is reached in the afternoon, rather than at noon.

Morrison [1970] summarized the microwave observations of Mercury obtained prior to 1970. These are disk-averaged brightness temperatures, at wavelengths between 0.3 and 11 cm. The most extensive data set is from Klein [1970]. He shows that the diurnal temperature variations indeed depend upon Hermographic longitude, with a minimum disk-averaged brightness temperature of ~300 K independent of longitude, and peak temperature between ~380 and ~440 K, depending on longitude. The best model to date has been developed by Cuzzi [1974]. He derived subsurface properties by comparing disk-averaged brightness temperatures at wavelengths between 0.3 and 18 cm. Mercury's surface appears similar to that of the moon. The top few centimeters consist of a low density ($\rho \sim 0.6$–1.0 g/cm^3) powder, with dielectric constant $\varepsilon \sim 1.5$–2. The density as well as ε increase with depth in the crust, to $\rho \sim 1.5$–2 g/cm^3, and $\varepsilon \sim 3$ at a depth of about 2.5 meters.

Radio images of the planet show a brightness variation across the disk, which displays the history of

the solar insulation. The first VLA images have been obtained by Chapman [1986] in April 1985, at 2 and 6 cm wavelength. In July 1986 Burns et al. [1987] observed the planet at 6 cm wavelength. Figure 27 shows the 6 cm image from Burns et al. [1987]. The planet had an eastern elongation 22°, and phase of 0.22. The viewing geometry of the planet, the Hermographic longitude of 0° and the equator, are indicated in the inset. Clearly, the disk shows an asymmetric brightness temperature distribution, with the hottest area centered near 0° longitude. In contrast to the radio images of Venus and Mars, no correlations between spatial brightness variations and known optical/infrared features on the surface of Mercury have been distinguished [Chapman 1986]. Figure 28 shows a preliminary image at 3 mm wavelength obtained with the Hat Creek Radio Interferometer [Mitchell et al. 1990], while the planet was at perihelion, and at greatest eastern elongation. A large day-to-night difference in temperature is readily visible.

At 6 cm we probe 0.5–1 m down into the surface, where the diurnal temperature variation at any longitude is minimal. If the thermal properties such as albedo, emissivity, thermal inertia and loss tangent do not vary across the disk, any spatial variations in the brightness temperature across the disk must be due to variations in the physical temperature at these depths. Burns et al. [1987] show that the observed brightness temperature variations at 6 cm indeed more or less mimic the spatial variations expected from the nonuniform heating of the planet. Chapman's images show the nightside of Mercury, at longitudes ~180° away from the picture of Burns et al. Also in Chapman's 6 cm data the region at a longitude near ~180° is clearly warmer than the surroundings.

At 3 mm wavelength one probes only a few centimeters into the crust, where the diurnal temperature variation is relatively large. Since in fig. 28 Hermographic longitude 0° coincides with local noon at the planet, the brightness temperature should be maximal at this longitude, ~500–600 K [see Mitchell et al. 1990]. The temperature at midnight should be much smaller, ~200 K. The coldest area on the disk coincides with the subearth point and the 6 AM meridian. The brightness temperature of this region will

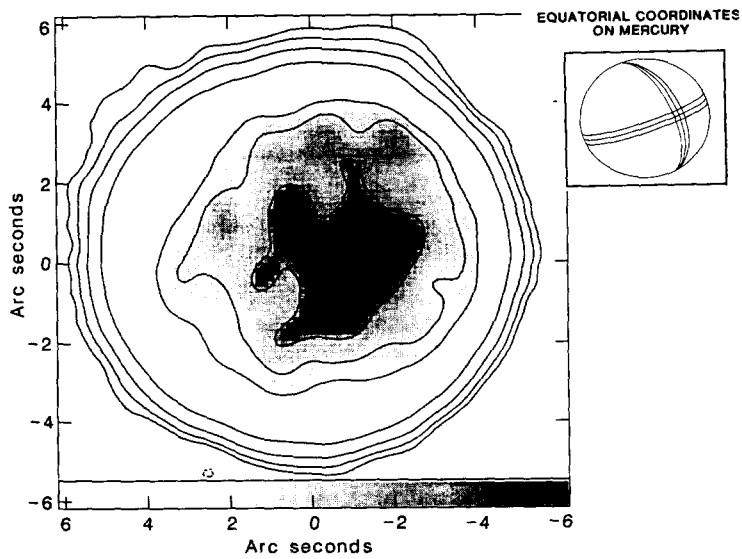

Fig. 27. Radio image of Mercury at 6 cm wavelength (from Burns et al. [1987]). Contour levels are: 20, 40, 80, 160, 310, 330, 350, and 370 K. In the upper right corner the geometry of the planet is shown, with the equator, circles of latitude ±5°, and meridians of longitude 0° and ±5°. The FWHP of the beam is 1".

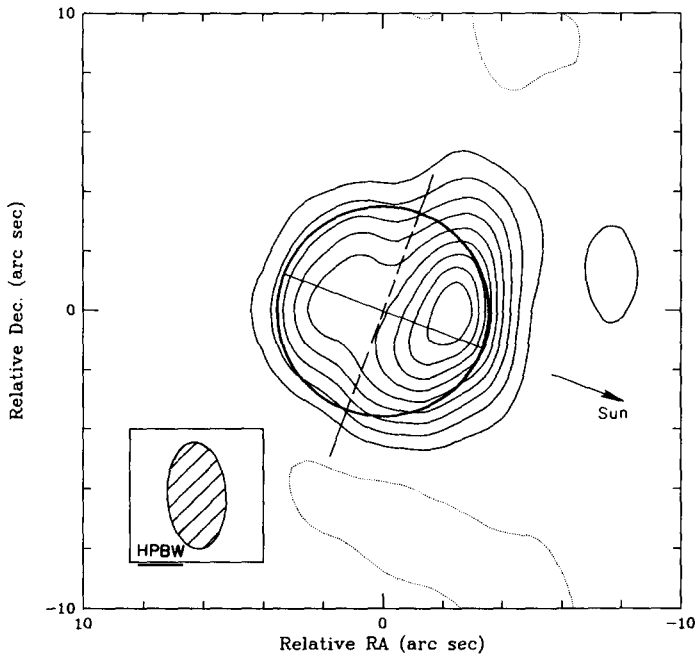

Fig. 28. Preliminary radio image of Mercury at 3 mm (from Mitchell, de Pater and Wright, in preparation). Contour levels are at 10% intervals. The direction to the sun, the size of the disk, the terminator and the HPBW are indicated. The subsolar longitude is at 0°.

probably be slightly less than that at $\phi = 180°$. The 3 mm image indeed shows these temperature variations; detailed simulations are still in progress however.

3.5. Conclusions

Microwave observations of the terrestrial planets have considerably improved our knowledge regarding their (sub)surface layers and atmospheres. The surface of these planets is typically overlain by a few centimeters of dust. The polar regions on Mars are much colder than the surrounding areas, probably due to the presence of CO_2 frost on the surface. The highlands on Venus have a lower emissivity and hence higher dielectric constant than the disk-averaged value; this implies the presence of substantial amounts of minerals and sulfides close to the surface. Mercury exhibits "hot spots" in its subsurface layers, due to the 3/2 orbital resonance and large orbital eccentricity.

Observations at millimeter wavelengths, in particular in the rotational transitions of the CO line, are used to derive the temperature gradient in Venus and Mars' atmospheres, and the CO abundance as a function of altitude. The CO abundance on Mars is much lower than expected from recombination of CO and O. Recombination might be increased by the presence of odd hydrogen or aerosols in the atmosphere. The CO abundance might be variable in time on timescales as short as 10 days. On Venus large differences in the CO line profile between the dayside and nightside are seen; deep narrow lines on the nightside, and broad lines which are about three times less deep on the dayside. Hence, the CO abundance on the nightside is much larger than that on the dayside, despite the fact that CO is produced in the dayside hemisphere by photolysis of CO_2. Large thermal winds may carry the CO from the dayside to the nightside.

4. Future research

With the radio detection of Pluto [Altenhoff et al. 1988] all planets have now been detected at radio wavelengths, and most of them have been imaged as well, as described in this review. By no means does this imply that this type of research has been completed; rather, it serves as a first step to identify the important issues which can be addressed through radio imaging of planets. In the future the following topics should be addressed in detail: (a) a physical explanation for the detailed structure seen in images of Jupiter's synchrotron radiation, and the time variations therein; (b) detailed dynamical modeling of the planetary atmospheres and comparison with multiwavelength radio images obtained over a significant time interval; (c) extraction of longitudinal information from images of the giant planet atmospheres employing improved deconvolution techniques; (d) search for minor constituents in the giant planet atmospheres, such as HCN, SO_2, CO, PH_3; (e) study of Saturn's rings and comparison with Voyager data; (f) detailed imaging and modeling of the atmospheres and surfaces of the terrestrial planets.

Of particular interest would be the simultaneous imaging of the $J = 1$–0, and 2–1 rotational transitions of both ^{12}CO and ^{13}CO on Venus and Mars at different locations in their orbits. Furthermore, to best constrain thermophysical models of Mercury's subsurface layers, images at infrared-to-centimeter wavelengths are required at different orbital positions and subearth longitudes. Observations at millimeter wavelengths are possible with the OVRO and HCRO arrays. The latter is particularly suitable for planetary research because of its large field of view and good instantaneous UV coverage in its future expanded configuration (of nine dishes).

Acknowledgements

Over the years I have worked with a number of collaborators on various aspects of research described in this review, e.g., S.K. Atreya, J.R. Dickel, C.K. Goertz, S. Gulkis, M.J. Klein, S.T. Massie, D. Mitchell, M. Richmond, P.N. Romani, and F.P. Schloerb. I would like to thank them for their contributions to this work. I further appreciate comments on this manuscript by S.K. Atreya, B.D. Chapman, J.R. Dickel, D. Mitchell, F.P. Schloerb and P.G. Steffes. I further like to thank D.J. Rudy for letting me use his (unpublished) image of Mars. The research described in this paper is supported by NSF grants AST-8514896 and AST-8900156 and NASA grant NAGW-1805 to the University of California in Berkeley, and the Alfred P. Sloan Foundation.

References

Acuna, M.H. and N.F. Ness, 1976, in: Jupiter, ed. T. Gehrels (Univ. of Arizona Press, Tucson) pp. 830–847.
Altenhoff, W.J., R. Chini, H. Hein, E. Kreysa, P.G. Mezger, C. Salter and J.B. Schraml, 1988, Astron. Astrophys. 190, L15–17.
Andrew, B.H., G.A. Harvey and F.H. Briggs, Astrophys. J. 213, L131–L134; 1978, Astrophys. J. 220, L61 (erratum).
Atreya, S.K. and J.E. Blamont, 1990, Geophys. Res. Lett. 17, 287–291.
Berge, G.L., 1966, Astrophys. J. 146, 767–798.
Berge, G.L. and S. Gulkis, 1976, in: Jupiter, ed. T. Gehrels (Univ. of Arizona Press, Tucson) pp. 621–692.
Berge, G.L., D.O. Muhleman and R. Linfield, 1988, Astronom. J. 96, 388–395.
Bezard, B., D. Gautier and B. Conrath, 1984, Icarus 60, 274–288.
Bolton, S.J. S. Gulkis, M.J. Klein, I. de Pater and T.J. Thompson, 1989, J. Geophys. Res. 94, 121–128.
Branson, N.J.B.A., 1968, Mon. Not R. Astron. Soc. 139, 155–162.

Briggs, F.H., 1974, Astrophys. J. 189, 367–377.
Briggs, F.H. and B.H. Andrew, 1980, Icarus 41, 269–277.
Briggs, F.H. and P.D. Sackett, 1989, Icarus 80, 77–103.
Burke, B.F. and K.L. Franklin, 1955, J. Geophys. Res. 60, 213.
Burns, J.O., G.R. Gisler, J.E. Borovsky, D.N. Baker and M. Zeilik, 1987, Nature 329, 234–236.
Campbell, M.J. and J. Ulrichs, 1969, J. Geophys. Res. 74, 5867–5881.
Carlson, B.E., A.A. Lacis and W.B. Rossow, 1988, Bull. Am. Astron. Soc. 20, 869.
Carr, T.D. and M.D. Desch, 1976, in: Jupiter, ed. T. Gehrels (Univ. of Arizona Press, Tucson) pp. 693–737.
Carr, T.D., M.D. Desch and J.K. Alexander, 1983, in: Physics of the Jovian Magnetosphere, ed. A.J. Dessler (Cambridge Univ. Press, Cambridge) pp. 226–284.
Chapman, B.D., 1986, Ph.D. Dissertation, Massachusetts Institute of Technology, Massachusetts.
Clancy, R.T., 1983, Ph.D. Thesis, California Institute of Technology, Pasadena, California.
Clancy, R.T. and D.O. Muhleman, 1985, Icarus 64, 183–204.
Clancy, R.T., D.O. Muhleman and B.M. Jakosky, 1983, Icarus 55, 282–301.
Conrath, B., D. Gautier, R. Hanel, G. Lindal and A. Marten, 1987, J. Geophys. Res. 92, 15003–15010.
Courtin, R., N. Coron, T. Encrenaz, R. Gispert, P. Bruston, G. Leblanc, G. Dambier and A. Vidal-Madjar, 1977, Astron. Astrophys. 60, 115–123.
Courtin, R., D. Gautier, A. Marten, B. Bezard and R. Hanel, 1984, Astrophys. J. 287, 899–916.
Cuzzi, J.N., 1974, Astrophys. J. 189, 577–586.
Cuzzi, J.N. and W.A. Dent, 1975, Astrophys. J. 198, 223–227.
Cuzzi, J.N., J.B. Pollack and A.L. Summers, 1980, Icarus 44, 683–705.
De Pater, I., 1980, Astron. Astrophys. 88, 175–183.
De Pater, I., 1981a, J. Geophys. Res., 86, 3397–3422.
De Pater, I., 1981b, J. Geophys. Res., 86, 3423–3429.
De Pater, I., 1983, Adv. Space Res. 3 (3), 31–37.
De Pater, I., 1985, ESA SP-241, in: Proc. inter. workshop (Alpbach, Austria, September 1985) pp. 203–208.
De Pater, I., 1986, Icarus, 68, 344–365.
De Pater, I., 1990, Annu. Rev. Astron. Astrophys. 28, 347–399.
De Pater, I. and H.A.C. Dames, 1979, Astron. Astrophys. 72, 148–160.
De Pater, I. and J.R. Dickel, 1982, Icarus, 50, 88–102.
De Pater, I. and J.R. Dickel, 1983, Adv. Space Res. 3 (3), 39–41.
De Pater, I. and J.R. Dickel, 1986, Astrophys. J., 308, 459–471.
De Pater, I. and J.R. Dickel, 1989, in preparation.
De Pater, I. and C.K. Goertz, 1989, Geophys. Res. Lett. 16, 97–100.
De Pater, I. and C.K. Goertz, 1990, J. Geophys. Res., 95, 39–50.
De Pater, I. and S. Gulkis, 1988, Icarus 75, 306–323.
De Pater, I. and W.J. Jaffe, 1984, Astrophys. J. Suppl. 54, 405–419.
De Pater, I. and M.J. Klein, 1989, in: Proc. inter. workshop on Time variable phenomena in the Jovian system (Flagstaff, Arizona, August 1987) pp. 139–150.
De Pater, I. and S.T. Massie, 1985, Icarus 62, 143–171.
De Pater, I. and M. Richmond, 1989, Icarus, 80, 1–13.
De Pater, I., S. Kenderdine and J.R. Dickel, 1982, Icarus 51, 25–38.
De Pater, I., P.N. Romani and S.K. Atreya, 1989, Icarus 82, 288–313.
De Pater, I., F.P. Scloerb and A. Rudolph, 1990, Icarus, submitted.
Dowling, T.E., D.O. Muhleman and G.L. Berge, 1987, Icarus 70, 506–516.
Epstein, E.E., M.A. Janssen, J.N. Cuzzi, W.G. Fogarti and J. Motman, 1980, Icarus 41, 103–108.
Epstein, E.E., B.H. Andrew, F.H. Briggs, B.M. Jakosky and F.D. Palluconi, 1983, Icarus 56, 465–475.
Epstein, E.E., M.A. Janssen and J.N. Cuzzi, 1984, Icarus 58, 403–411.
Esposito, L.W., R.G. Knollenberg, M.Ya. Marov, O.B. Toon and R.P. Turco, 1983, in: Venus, eds D.M. Hunten, L. Colin, T.M. Donahue and V.I. Moroz (Univ. of Arizona Press, Tucson) pp. 484–564.
Esposito, L.W., J.N. Cuzzi, J.B. Holberg, E.A. Marouf, G.L. Tyler and C.C. Porco, 1984, in: Saturn, ed. T. Gehrels (Univ. of Arizona Press, Tucson) pp. 463–545.
Flasar, F.M., B.J. Conrath, P.J. Gierasch and J.A. Piraglia, 1987, J. Geophys. Res. 92, 15 011–15 018.
Gerard, E., 1970, Radio Sci. 5, 513–516.
Gerard, E., 1976, Astron. Astrophys. 50, 353–360.
Goldstein, J.J., M.J. Mumma, T. Kostiuk, D. Deming, F. Espenak and D. Zipoy, 1988, Bull. Am. Astron. Soc. 20, 833.
Good, J.C. and F.P. Schloerb, 1981, Icarus 47, 166–172.
Grossman, A.W., D.O. Muhleman and G.L. Berge, 1989, Science 245, 1211–1215.
Gulkis, S. and I. de Pater, 1984, NASA Conf. Publ. 2330, in: Proc. workshop (Pasadena, CA, February 1984) pp. 225–262.

Gulkis, S., M.J. Janssen and E.T. Olsen, 1978, Icarus 34, 10–19.
Gulkis, S., E.T. Olsen, M.J. Klein and T.J. Thompson, 1983, Science 221, 453–455.
Hofstadter, M.D. and D.O. Muhleman, 1989, Icarus, 81, 396–412.
Hubbard, W.B., 1984, Planetary interiors (Van Nostrand/Reinhold, New York).
Hunten, D.M., 1974, Rev. Geophys. Space Phys. 12, 529–535.
Jaffe, W.J., 1977, unpublished preprint.
Jaffe, W.J., G.L. Berge, T. Owen and J. Caldwell, 1984, Science 225, 619–621.
Janssen, M.A. and E.T. Olsen, 1977, Icarus 33, 263–278.
Kakar, R.K., J.W. Waters and W.J. Wilson, 1976, Science 191, 379–380.
Kellermann, K.I. and I.I.K. Pauliny-Toty, 1966, Astrophys. J. 145, f954–957.
Klein, J.J., 1970, Radio Sci. 5, 397.
Klein, M.J., 1984, private communication.
Klein, M.J., 1976, J. Geophys. Res. 81, 3380–3382.
Klein, M.J. and S. Gulkis, 1978, Icarus 35, 44–60.
Klein, M.J. and J.A. Turegano, 1978, Astrophys. J. 224, L31–34.
Klein, M.J., S. Gulkis and C.T. Stelzried, 1972, Astrophys. J. 176, L85–L88.
Klein, M.J., M.A. Janssen, S. Gulkis and E.T. Olsen, 1978, in: The Saturn System, NASA conf. publ. 2068, pp. 195–216.
Klein, M.J., T.J. Thompson and S.J. Bolton, 1989, in: Proc. inter. workshop on Time variable phenomena in the Jovian System (Flagstaff, Arizona, August 1987).
Kraus, J.D., 1986, Radio Astronomy (Cygnus Quasar Books, Powell, Ohio).
Lellouch, E., M. Gerin, F. Combes, S.K. Atreya and T. Encrenaz, 1989, Icarus 77, 414–438.
Lewis, J.S., 1969, Icarus 10, 365–378.
Lindal, G.F., J.R. Lyons, D.N. Sweetnam, V.R. Eshelman, D.P. Hinson and G.L. Tyler, 1987, J. Geophys. Res. 92, 14 987–15 002.
Mayer, C.H., T.P. McCullough and R.M. Sloanaker, 1958, Astrophys. J. 127, 11–16.
Mitchell, D.L., I. de Pater and M.C.H. Wright, 1990, Icarus, in preparation.
Morris, D. and G.L. Berge, 1962, Astrophys. J. 136, 276–282.
Morrison, D., 1970, Space Sci. Rev. 11, 271–307.
Muhleman, D.O., G.S. Orton and G.L. Berge, 1979, Astrophys. J. 234, 733–745.
Orton, G.S., K.H. Baines, J.T. Bergstrahl, R.H. Brown, J. Caldwell and A.T. Tokunaga, 1987, Icarus 69, 230–238.
Perley, R.A., F.R. Schwab and A.H. Bridle, 1989, in: Synthesis Imaging in Radio Astronomy, Proc. NRAO Workshop 21 (Astron. Soc. Pac., San Francisco).
Pettengill, G.H., P.G. Ford and B.D. Chapman, 1988, J. Geophys. Res. 93, No. B12, 14 881–14 892.
Pollack, J.B. and P. Bodenheimer, 1989, in: Origin and Evolution of Planetary and Satellite Atmospheres, eds S.K. Atreya, J.B. Pollack and M.S. Matthews (Univ. of Arizona Press, Tucson) pp. 564–602.
Radhakrishnan, V. and J.A. Roberts, 1960, Phys. Rev. Lett. 4, 493–494.
Rather, J.D.G., B.L. Ulich and P.A.R. Ade, 1974, Icarus 23, 448–453.
Roberts, J.A. and G.R. Huguenin, 1963, La Physique des planets 7, 569.
Roberts, J.A., G.L. Berge and R.C. Bignell, 1984, Astrophys. J. 282, 345–358.
Rolhfs, K., 1986, Tools of Radio Astronomy (Springer, Berlin).
Romani, P.N., 1986, Ph.D. Thesis, University of Michigan, Ann Arbor, Michigan.
Romani, P.N., I. de Pater and S.K. Atreya, 1989, Geophys. Res. Lett., 16, 933–936.
Rowan-Robinson, M., P.A.R. Ade, E.I. Robson and P.E. Clegg, 1978, Astron. Astrophys. 62, 249–254.
Rudy, D.J., 1987, Ph.D. Dissertation, California Institute of Technology, Pasadena, California.
Rudy, D.J., D.O. Muhleman, G.L. Berge, B.M. Jakosky and P.R. Christensen, 1987, Icarus 71, 159–177.
Schloerb, F.P., 1985, in: Proc. ESO-IRAM-Onsala workshop on (sub) millimeter astronomy (Aspenas, Sweden, June 1985).
Schloerb, F.P., 1978, Ph.D. dissertation, California Institute of Technology, Pasadena, California.
Schloerb, F.P., D.O. Muhleman and G.L. Berge, 1979, Icarus 39, 214–231.
Schloerb, F.P., D.O. Muhleman and G.L. Berge, 1980, Icarus 42, 125–135.
Seiff, A., 1983, in: Venus, eds D.M. Hunten, L. Colin, T.M. Donahue and V.I. Moroz (Univ. of Arizona Press, Tuscon) pp. 215–279.
Seiff, A. and D.B. Kirk, 1977, J. Geophys. Res., 82, 4364–4378.
Sloanaker, R.M., 1959, Astron. J. 64, 346.
Soter, S. and J. Ulrichs, 1967, Nature 214, 1315–1316.
Steffes, P.G., 1985, Icarus 64, 576–585.
Steffes, P.G., 1986, Astrophys. J. 310, 482–489.
Steffes, P.G. and J.M. Jenkins, 1987, Icarus 72, 35–47.
Steffes, P.G., M.J. Klein and J.M. Jenkins, 1990, Icarus 84, 83–92.
Thompson, A.R., J.M. Moran and G.W. Swenson, 1986, Interferometry and Synthesis in Radio Astronomy (Wiley, New York).
Ulrich, B.L., 1974, Icarus 21, 254–261.
Werner, M.W., G. Neugebauer, J.R. Houck and M.G. Hauser, 1978, Icarus 35, 289–296.
West, R.A., D.F. Strobel and M.G. Tomasko, 1986, Icarus 65, 161–217.